



Regulation of acidity properties of ZSM-5 and proximity between metal oxide and zeolite on bifunctional catalysts for enhanced CO₂ hydrogenation to aromatics

Yihua Yue^{a,1}, Jian Tian^{b,1}, Jiechao Ma^a, Shui Yang^a, Wen Li^c, Jiale Huang^{a,*}, Qingbiao Li^{a,*}, Guowu Zhan^{b,*}

^a College of Chemistry and Chemical Engineering, Xiamen University, 422 Siming South Road, Xiamen, Fujian 361005, China

^b Academy of Advanced Carbon Conversion Technology, College of Chemical Engineering, Huaqiao University, 668 Jimet Avenue, Xiamen, Fujian 361021, China

^c College of Advanced Manufacturing, Fuzhou University, 1 Shui Cheng Road, Jinjiang, Fujian 362200, China

ARTICLE INFO

Keywords:

CO₂ hydrogenation
Bifunctional catalysts
Aromatics
ZSM-5 zeolites
Rice husk

ABSTRACT

Herein, Ga-ZnZrO_x&ZSM-5 bifunctional catalysts were designed for CO₂ thermal hydrogenation to aromatics, particularly, aiming to enhance the selectivity of high-value BTX (i.e., benzene, toluene, and xylene). It was evident that the exterior surface properties and acidity of ZSM-5 can be effectively tailored by *in-situ* silicon deposition originating from the rice husk template. Catalytic performance assessments demonstrate an optimized catalyst achieving 88.1 % aromatics selectivity (exclusive CO) in a single pass, with a notable 45.2 % BTX selectivity within total aromatics and a low CO selectivity of 23.6 %. This superior performance is attributed to the *in-situ* silicon deposition on ZSM-5 during one-pot synthesis and the optimized spacing between Ga-ZnZrO_x and ZSM-5 facilitated by the rice husk platform. Furthermore, *in-situ* DRIFTS analysis identifies key reaction intermediates. This study offers an effective strategy for tuning zeolite acidity using rice husks, while modulating metal oxide-zeolite proximity on the bio-SiO₂ platform, thus boosting CO₂ conversion to aromatics.

1. Introduction

The direct strategy that converts CO₂ with green hydrogen into high value-added aromatics (especially light aromatics, i.e., benzene, toluene, and xylene, BTX) over bifunctional catalysts has attracted increasing research interest. It may be a more viable and sustainable route than the traditional petroleum-based platform, considering the increasingly serious contradiction between the demand for aromatics and the depletion of petroleum [1,2]. Recently, encouraging progress has been made in converting CO₂ to aromatics and liquid hydrocarbons over bifunctional catalysts composed of diverse metals (or metal oxides) and ZSM-5 zeolites with ten-membered-ring (10MR) openings, such as ZnZrO/ZSM-5 [3], ZnAlO_x&ZSM-5 [4], Cr₂O₃/ZSM-5 [5], Na-Fe@C/ZSM-5 [6], ZnFeO_x-Na/S-ZSM-5 [7], In₂O₃/ZSM-5 [8], Na-Fe₃O₄/ZSM-5 [9], NaFe/SAPO-11/ZSM-5 [10], and so forth. In this tandem catalysis, the metallic component and zeolite component can be separately used for the methanol formation reaction and methanol to aromatics (MTA) reaction, respectively [11,12], hopefully breaking the

thermodynamic limitation of CO₂ hydrogenation (Fig. S1) [13,14]. In addition, to maximize the synergy of the two components, the compatibility (*viz.*, hydrogenation ability of metallic oxide, structure and acid properties of zeolites) and distance (*i.e.*, intimacy or proximity) of the two components are critical for the catalytic performance [15,16].

ZSM-5 zeolites with unique microcellular structures (the nearly circular cross-section of 0.51–0.56 nm diameter) and adjustable solid acid properties have been widely used as the preferred catalytic material in the petrochemical field [17]. Meanwhile, ZSM-5 is the most desirable shape-selective zeolite that exhibits very high selectivity toward para-xylene (*p*-xylene) as its channel matches the kinetic size of *p*-xylene (~0.58 nm). Theoretically, *p*-xylene is preferentially formed and faces the lowest diffusion hindrance through the zeolite framework [18]. Unfortunately, *p*-xylene is readily isomerized to ortho- or meta-xylenes and alkylated to heavier aromatics on the external surface acid sites of ZSM-5 zeolites, leading to a low selectivity to *p*-xylene [19]. Accordingly, precise tuning of pore size and acid distribution of ZSM-5 zeolite by complex modification method is necessary to improve catalytic

* Corresponding authors.

E-mail addresses: cola@xmu.edu.cn (J. Huang), kelqb@xmu.edu.cn (Q. Li), gwzhan@hqu.edu.cn (G. Zhan).

¹ These authors contributed equally to this work.

activity and the selectivity of light aromatics [20]. For example, Wang *et al.* reported the investigation of HZSM-5 with dominantly sinusoidal channel openings over its acid-sites-free external surface to achieve high *p*-xylene selectivity in toluene alkylation reaction [21]. Sun *et al.* reported that a proper extension of the *b*-axis length of HZSM-5 could increase the selectivity of *p*-xylene in CO₂ hydrogenation [22]. Despite the potential benefits, such modification methods pose significant challenges to the high cost and complex post-treatment procedures. Moreover, these methods often compromise the reactivity of the zeolite as modifiers might neutralize acid sites and partially disrupt its crystal structure, reducing the number of active sites [23].

To address this challenge, researchers have rationally utilized natural biomass as templates to develop diverse biomaterials with desirable textural structures, such as butterflies [24], rice husk [25], cotton [26], pollen [27], yeast [28], and bovine serum protein [29], *etc.* Recently, our group reported the fabrication of hierarchically structured zeolites with natural biological templates, which showed suitable acidity without requiring tedious modification processes [30,31]. For instance, rice husk was used as a green silicon source and template to prepare bio-SAPO-34 and bio-ZSM-5 with multiple mesostructures and moderate acid sites. This approach effectively addresses the issues of zeolite deactivation and pore blockage, resulting in impressive catalytic activity for CO₂ hydrogenation into light olefins and aromatics. It is noteworthy that rice husks are rich in green silicon sources as well as have abundant pores and hierarchical structures that are suitable for building catalytic materials. Additionally, rice husk is a low-cost waste agricultural by-product with *ca.* 100 million tons/year globally [32].

In addition to the construction of the desirable textural structures of the zeolite, in the CO₂ hydrogenation to aromatics, the intermediate products (such as methanol and ketene) must be consumed rapidly; therefore, the spatial distance (*i.e.*, proximity) between the bifunctional sites is also critical to the tandem catalysis process [33]. Hitherto, the current integration manners of bifunctional components, are limited to specific methods: dual-bed mode with millimeter-scale spacing, granule-mixing method with hundreds of micrometers spacing, powder/mortar-mixing method with nanometer-scale spacing, and the core-shell structure with metal oxide encapsulated inside zeolites. Numerous studies have found that CO₂ conversion and aromatic selectivity increase with closer proximity between the two components [34]. However, the high proximity might lead to the deactivation of the zeolite because of the easy migration of metal ions to the zeolite and the deep alkylation of BTX into polyalkylbenzenes and polycyclic aromatic hydrocarbons (PHA, the coke precursor) covering the acidic sites of the zeolite [35,36]. In this regard, it has been found that mixing MFI zeolites with inert binders (*i.e.*, SiO₂) effectively reduced the possibility of product molecules re-entering the adjacent zeolites to undergo repeated diffusion/reaction [37,38]. Inspired by this, biomass templates with hierarchically porous structures can not only provide a unique platform for the assembly of bifunctional components but also promote product diffusion. However, quantitatively describing the correlation between

proximity and catalytic performance is quite difficult [39]. Recently, Li *et al.* discovered that the distance effect on the communication between metal sites and acid sites in a methanol-mediated syngas conversion system and the Péclet (*Pe*) number was employed to assess the maximum diffuse distance of methanol intermediates in the catalyst bed [40]. Unfortunately, there is still a lack of work to comprehensively understand how dual-component proximity relates to tandem catalysis, as well as to rationalize catalyst layout to maximize catalysis efficiency.

In this work, as illustrated in Scheme 1, we introduce a facile preparation method for Ga-ZnZrO_x&ZSM-5 bifunctional catalysts with rice husk as a green silicon source and template, which can inherit the hierarchical structure of rice husk. The performance of the designed bifunctional catalysts for direct CO₂ thermal hydrogenation into aromatics was evaluated. Interestingly, the rice husk-derived SiO₂ (bio-SiO₂) could serve as a platform for the integration of metal oxide and zeolite components. Rather than post modifications that improve zeolite shape-selectivity at the cost of stability and reactivity, *in-situ* silicon deposition on zeolites derived from rice husks effectively prevented the reduction of the effective surface area and active sites of ZSM-5, resulting in enhanced selectivity for BTX. In addition, semi-empirical relation (including specific surface area, particle size, loading amount, *etc.*) was established for the quantitative analysis of the proximity between metal oxide and zeolite (the dimensionless number *lnP*), and a strong correlation between proximity and BTX selectivity was obtained by modulating the two-component distance using bio-SiO₂ platform. Moreover, no significant deactivation of the bifunctional catalyst was observed for at least 150 h on stream at 340 °C, being promising for industrial applications.

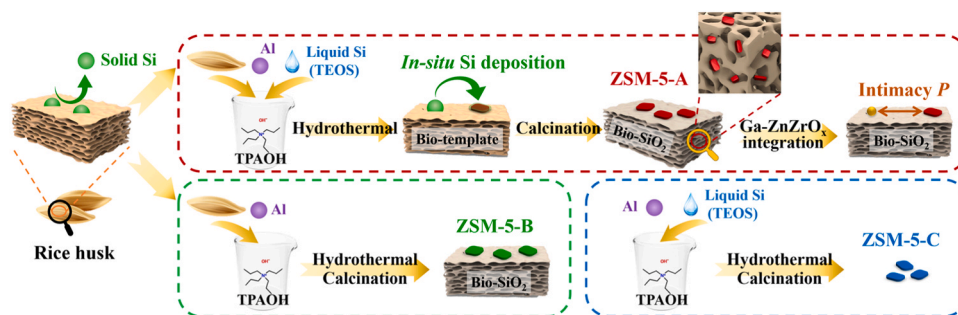
2. Experimental section

2.1. Chemicals and raw materials

The following reagents were used without further purification: zinc nitrate hexahydrate (Zn(NO₃)₂·6H₂O, AR), tetraethyl orthosilicate (TEOS, AR), ammonia solution (NH₄OH, AR) and hydrochloric acid (HCl, AR) were purchased from Sinopharm Chemical Reagent Co. Ltd. Zirconium nitrate pentahydrate (Zr(NO₃)₄·5H₂O, 99.99 %) was purchased from Macklin Chemicals Co. Ltd. Gallium nitrate hydrate (Ga(NO₃)₃·xH₂O, 99.9 %) and sodium aluminate (NaAlO₂, 99.5 %) were purchased from Aladdin Chemical Reagent Company. Tetrapropylammonium hydroxide (TPAOH, 40 wt% in water) was purchased from Energy Chemical Co. Ltd. The natural rice husk was bought from a farmer in Xiamen, Fujian Province, China. Deionized water was used for all experiments.

2.2. Pretreatment of rice husk

First, the natural rice husk was soaked in 1.4 mol L⁻¹ (5 wt%) HCl solution for one day, washed with deionized water to get the filtrate



Scheme 1. Schematic illustration of the preparation routes of ZSM-5 zeolite (ZSM-5-A) by using rice husk as a silicon source and template. Notes: As a comparison, ZSM-5-B zeolite was prepared without the conventional chemical silicon species (TEOS), and ZSM-5-C zeolite was prepared by traditional methods without rice husk, with identical hydrothermal and calcination conditions. Particularly, Ga-ZnZrO_x and ZSM-5-A are integrated on the bio-SiO₂ platform with varying proximity.

solution pH of 7, separated by filtration, and dried at 80 °C overnight. Then, the soaked rice husk and 5 wt% HCl solution were added to the flask according to a certain liquid-material ratio, heated to a slightly boiling and condensed reflux for 4 h. After cooling to room temperature, the filtered rice husk was washed with distilled water to get the filtrate solution pH of 7 and dried at 80 °C overnight, and then stored in a dryer for subsequent use. The acid treatment was used to increase the purity of the SiO₂ (viz., bio-SiO₂, obtained after calcination treatment) by removing alkali and alkaline-earth elements such as K⁺, Ca²⁺, Na⁺, and other impurities (Figs. S2 and S3). In particular, by calcination treatment at 550 °C to remove the organic matter, the main chemical composition of the bio-SiO₂ platform was higher than 99 wt% SiO₂ (Table S1), and the surface area increased by more than ten times compared to that of the untreated one (Table S2).

2.3. Catalyst preparation methods

ZnZrO_x oxide with Zn/(Zn+Zr) molar percentage approaching 13 % was prepared via the reverse co-precipitation method. In a typical experiment, 0.77 g of Zn(NO₃)₂·6H₂O and 7.47 g of Zr(NO₃)₄·5H₂O were dissolved into 100 mL of deionized water. Subsequently, the mixture was added dropwise to 8 mL of NH₄OH, after which the suspension was continuously stirred for 2 h at 70 °C. When the aforementioned suspension was cooled to room temperature, the product was recovered by filtering, washing to get the filtrate solution pH of 7, drying (80 °C, 12 h), and calcination in the air at 520 °C for 5 h (with a heating rate of 2 °C min⁻¹). M-ZnZrO_x oxides (M = Ga, In, Sr, Co, Ni, Mg, and Al) were also synthesized by the reverse co-precipitation method as mentioned for the synthesis of the ZnZrO_x catalyst above. The molar percentage of Zn/(M+Zn+Zr) over M-ZnZrO_x oxides was fixed at 13 %. After replacing part amount of Zr(NO₃)₄·5H₂O with other metal nitrates, a series of different M-ZnZrO_x oxides were prepared. In this work, M-ZnZrO_x was the abbreviation for the M-ZnZrO_x oxides with a M/(M+Zn+Zr) molar percentage of 5 % unless otherwise mentioned.

MFI zeolite with different SiO₂/Al₂O₃ ratios was synthesized by hydrothermal synthesis in the presence of the pretreated rice husks with the molar ratio of 1 SiO₂: x Al₂O₃: 1.7 TPAOH: 136 H₂O (x = 0.01–0.1). Typically, 2.5 g of TEOS, 0.0984 g of NaAlO₂, 10.2 g of TPAOH (40 wt %), and 28.8 g of deionized water were mixed uniformly, and 5 g of above-dried pretreated rice husk was added. The mixture was stirred at room temperature for 12 h and sealed in a 100 mL Teflon-lined stainless-steel autoclave for zeolite crystallization at 170 °C under autogenic pressure for 12 h. After crystallization, as-synthesized samples were obtained after centrifugal separation, washing, and drying at 80 °C for 12 h. Next, the dried sample was calcined at 550 °C for 6 h with a rate of 2 °C min⁻¹ to remove the organic template and bio-components and obtain the Na-ZSM-5 product. Finally, to convert the Na-ZSM-5 to H-ZSM-5, the calcined Na-ZSM-5 was ion-exchanged (three times) with 0.2 mol L⁻¹ NH₄NO₃ aqueous solution at 80 °C for 3 h, and the product was subsequently calcined at 550 °C for 6 h. The obtained catalysts were denoted as H-ZSM-5-A. By adjusting the amount of NaAlO₂, H-ZSM-5-A with different SiO₂/Al₂O₃ ratios could be synthesized by the same method. For comparison, H-ZSM-5-B was synthesized without TEOS, and H-ZSM-5-C was synthesized without rice husk by the hydrothermal synthesis as mentioned for the synthesis of the H-ZSM-5-A zeolite above. In this work, ZSM-5-A, ZSM-5-B, and ZSM-5-C were the abbreviation for the H-ZSM-5-A zeolite with SiO₂/Al₂O₃ ratio of 64, the H-ZSM-5-B zeolite with SiO₂/Al₂O₃ ratio of 61 and the H-ZSM-5-C zeolite with SiO₂/Al₂O₃ ratio of 30, respectively, unless otherwise mentioned. It should be noted that the SiO₂/Al₂O₃ ratio here consists of ZSM-5 and bio-SiO₂ and the data is obtained from the TG analysis (Fig. S3a) and XRF (Table S1) of rice husks.

The mass ratio of M-ZnZrO_x oxide and ZSM-5 zeolite in this work was fixed at 1:2. The fine M-ZnZrO_x and ZSM-5 zeolite powders were mixed uniformly with an agate mortar for 10 min to obtain the bifunctional catalysts, denoted as M-ZnZrO_x/ZSM-5.

2.4. Catalyst characterization methods

The morphology, structure, and surface chemistry of the catalysts were characterized using *e.g.* SEM, XRD, N₂-physisorption, XRF, Ar-ion sputtering XPS, NH₃-TPD, Py-FTIR, ²⁷Al MAS NMR, TG, GC-MS, and *in-situ* DRIFTS, *etc.*, as described in the Supplementary Information.

2.5. Catalyst evaluation methods

The CO₂ conversion over the prepared catalysts was performed in a quartz flow tube placed in a high-pressure fixed-bed reactor. Typically, a 300 mg bifunctional catalyst composed of 100 g M-ZnZrO_x and 200 g ZSM-5 was loaded in a reactor (inner diameter, 8 mm). Prior to the reaction, the catalyst was activated in the reactor with an H₂ flow (20 mL min⁻¹) at 300 °C for 2 h, followed by being exposed to 30 bar of mixed feed gas (CO₂:H₂ = 1:3) with a space velocity of 6000 mL g_{cat}⁻¹ h⁻¹ at 340 °C. The reactants and the gaseous products generated after the reaction were analyzed by online gas chromatography (GC-9160) equipped with a flame ionization detector (FID) and thermal conductivity detector (TCD). PLOT. Q and JN-SE-54 capillary columns connected to two FID were used to analyze C₁–C₅ hydrocarbons and C₆–C₁₀ aromatics, respectively. Other gas products such as CO₂ and CO were separated by a TDX-01 packed column and detected by TCD. The CO₂ conversion and the product selectivity were calculated using Eqs. 1 to 4 with an internal normalization method.

CO₂ conversion was calculated on a carbon-atom basis, as follows:

$$\text{CO}_2 \text{ conversion}(\%) = \frac{f_{\text{CO}_2\text{A}_{\text{CO}_2}} + i \sum n f_{\text{C}_n\text{H}_m} A_{\text{C}_n\text{H}_m}}{f_{\text{CO}_2\text{A}_{\text{CO}_2}} + f_{\text{COA}_{\text{CO}}} + i \sum n f_{\text{C}_n\text{H}_m} A_{\text{C}_n\text{H}_m}} \times 100\% \quad (1)$$

where *f* is relative mole correction factor and *A* is peak area on chromatographic spectra at the reactor outlet. Hydrocarbon products (C_nH_m) include CH₄, C₂–C₄, C₅+, and aromatics.

$$i = \frac{f_{\text{CH}_4(\text{TCD})} A_{\text{CH}_4(\text{TCD})}}{f_{\text{CH}_4(\text{FID})} A_{\text{CH}_4(\text{FID})}} \quad (2)$$

where *i* is internal normalization conversion coefficient.

CO selectivity and hydrocarbon products (*i.e.* C_nH_m) selectivity (exclusive CO) were calculated, as follows:

$$\text{CO selectivity}(\%) = \frac{f_{\text{COA}_{\text{CO}}}}{f_{\text{COA}_{\text{CO}}} + i \sum n f_{\text{C}_n\text{H}_m} A_{\text{C}_n\text{H}_m}} \times 100\% \quad (3)$$

$$\text{C}_n\text{H}_m \text{ selectivity}(\%) = \frac{n f_{\text{C}_n\text{H}_m} A_{\text{C}_n\text{H}_m}}{\sum n f_{\text{C}_n\text{H}_m} A_{\text{C}_n\text{H}_m}} \times 100\% \quad (4)$$

The space-time yield (STY, mg of CH produced per gram catalyst per hour) for aromatics was calculated according to:

$$\text{STY(Aromatics)} = \frac{M_{\text{CH}} * F_{\text{CO}_2} * \text{CO}_{2(\text{Conv.})} * (1 - S_{\text{CO}}) * S_{\text{Aro.}}}{V_m * g_{\text{cat}}} \quad (5)$$

where *M*_{CH} is the molar mass of -CH-, *F*_{CO₂} is the gas volume flow rate of CO₂, *V*_m is the molar volume of the gas, *g*_{cat} is the mass of bifunctional catalysts.

3. Results and discussion

3.1. Characterization of zeolite prepared using biomass

Besides ZSM-5-A, ZSM-5-B was prepared without liquid silicon species (*viz.*, TEOS), and ZSM-5-C was prepared by traditional methods. Initially, the surface morphology and crystal size of ZSM-5 zeolites were examined by SEM images and EDX elemental maps (Fig. 1 and Figs. S4–6). As observed from the SEM images (Fig. 1a,b) at low magnifications, all the ZSM-5 particles were uniformly dispersed on the

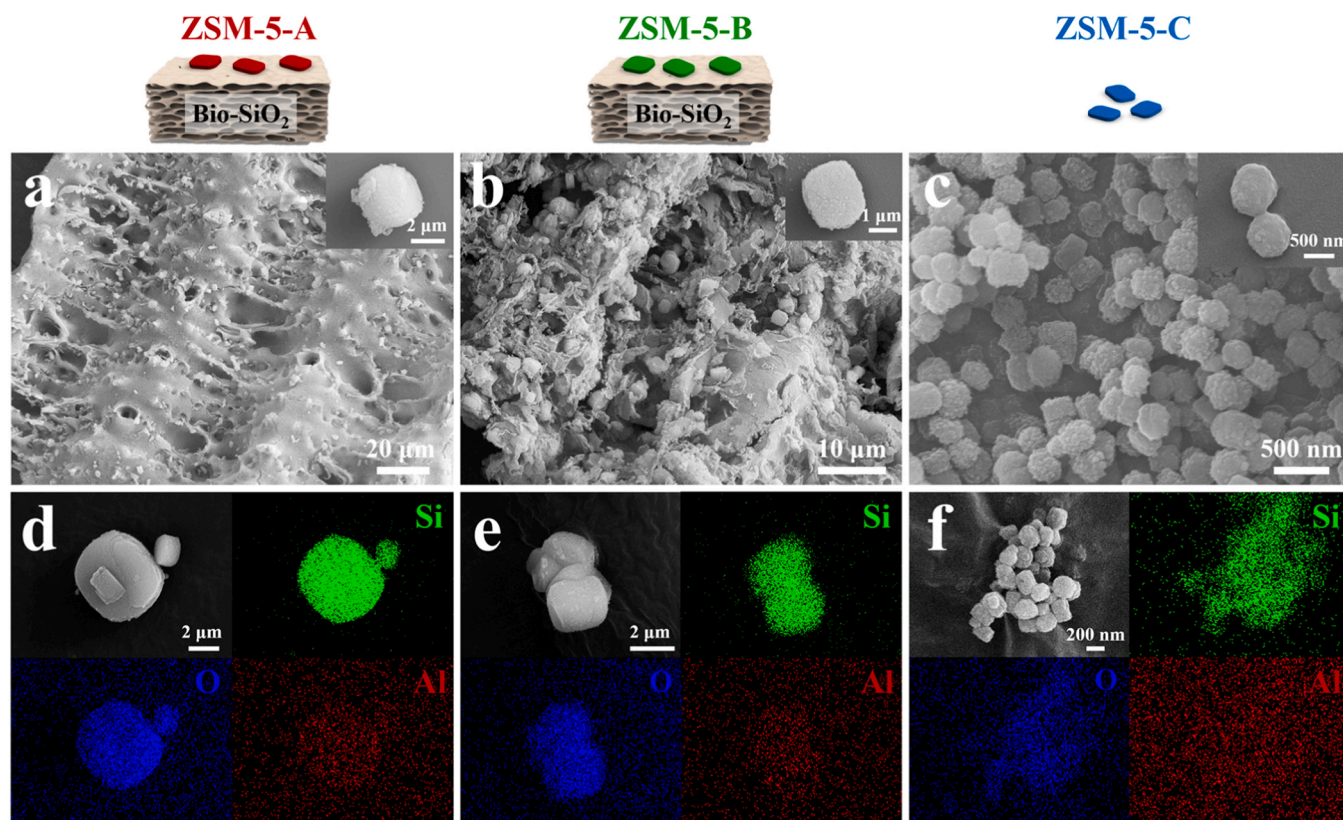


Fig. 1. Representative SEM images of (a) ZSM-5-A, (b) ZSM-5-B, and (c) ZSM-5-C and the corresponding insets show the enlarged images of the single particle. EDX elemental maps of (d) ZSM-5-A, (e) ZSM-5-B, and (f) ZSM-5-C samples.

surface and pore channels of bio-SiO₂. In this case, the bio-SiO₂ with high purity of SiO₂ (99.7 wt%) is used as a platform (rather than a spacer) to adjust the spatial distance of the ZSM-5 particles. In contrast, without the addition of a bio-SiO₂ platform, ZSM-5-C particles are densely packed and overlapping (see Fig. 1c). All the ZSM-5 particles possess characteristic elliptical cuboid morphology at high magnifications. The morphology of ZSM-5 with rice husk providing the silicon source remained essentially unchanged compared to ZSM-5-C with a particle size of about 1 μm, whereas the particle sizes of ZSM-5-A and ZSM-5-B increased to 2–3 μm due to the large content and slow release of solid silicon source (*viz.*, rice husk). EDX elemental maps demonstrated that silicon species of rice husk enter zeolite to participate in its nucleation and crystallization, especially ZSM-5-B (Fig. 1e), which had

only silicon species from rice husk (without adding TEOS). In particular, the distribution of Si elements showed that the Si content on the surface of ZSM-5-A zeolite increased significantly, as compared to the other two samples (Fig. 1d).

Fig. 2a shows the XRD patterns of ZSM-5 zeolites with characteristic diffraction peaks assigned to typical MFI structures (JCPDS cards 44-0003) without any impurities in the range of 5–50° [41]. XRD patterns further proved the successful synthesis of ZSM-5 zeolites from a rice husk silicon source. N₂ isothermal adsorption-desorption isotherms and pore size distribution analyzed from the BJH adsorption branch of the various ZSM-5 zeolites are shown in Fig. 2b and Table S3. According to the IUPAC classification system, these three ZSM-5 zeolites exhibit typical type-IV isotherm with an H4-type hysteresis loop at a higher

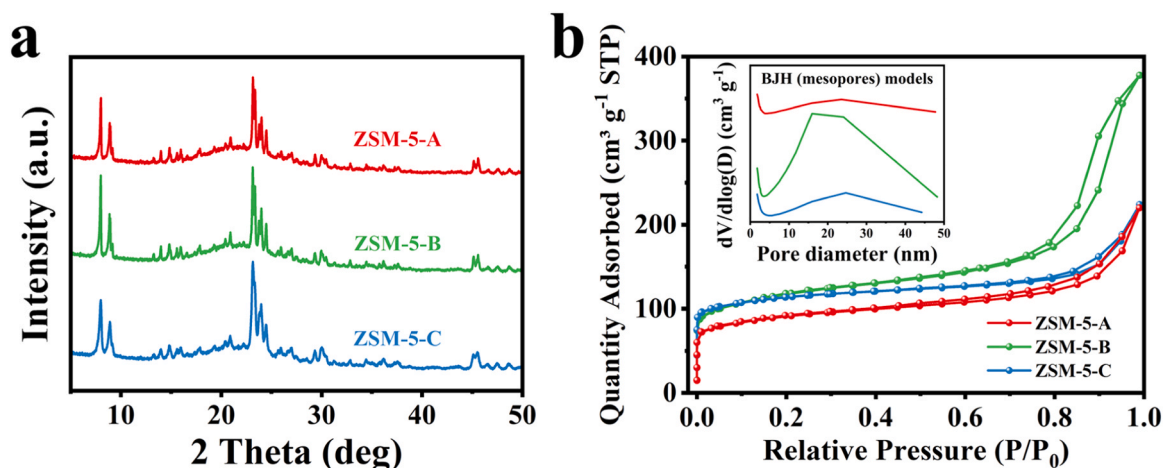


Fig. 2. (a) XRD patterns, (b) N₂ isothermal adsorption-desorption curves, and pore size distribution plots from the BJH model of ZSM-5-A, ZSM-5-B, and ZSM-5-C.

relative pressure, indicating that the samples possessing both mesoporous and microporous structures [42]. Significantly, the adsorption curves of ZSM-5-A and ZSM-5-B zeolites at relative pressures of 0.4–0.9 show more pronounced hysteresis loops, indicating the presence of a considerable amount of mesopores generated from bio-SiO₂. Meanwhile, ZSM-5-B has a larger external surface area (382.6 vs. 359.5 m² g⁻¹) and pore capacity (0.58 vs. 0.35 cm³ g⁻¹) compared to ZSM-5-C (Table S3), which is attributed to the coexistence of mesopores and macropores during the introduction of bio-SiO₂.

3.2. Evaluation of the catalytic activity of CO₂ hydrogenation

Since the activity of metal oxides is critical to the activity of bifunctional catalysts, we further investigated the effect of metal promoters (e.g., alkaline-earth metals and transition metals) on catalytic behaviors of M-ZnZrO_x (M = Ga, In, Sr, Co, Ni, Mg, and Al, labeled M-ZZ in Fig. 3a, b) catalysts for CO₂ hydrogenation to methanol. As shown in Fig. 3a, the XRD diffraction peaks of M-ZnZrO_x catalysts are consistent with the ZnZrO_x solid solution catalyst, indicating that the incorporation of metal promoters does not change the crystalline structures of catalysts. The metal promoters may exist in a highly dispersed state on the

ZnZrO_x solid solutions [43]. Among the various catalysts, the Ga-promoted ZnZrO_x solid solution catalyst (Ga-ZnZrO_x) exhibits the highest methanol STY of 352.7 mg g_{cat}⁻¹ h⁻¹ at 340 °C (see Fig. 3b and Table S4). This was attributed to the introduction of Ga to further enhance the H₂ heterolytic activation while generating more oxygen vacancies (i.e. defect oxygen, O_{defect}), thus facilitating the methanol yield over the solid solution catalysts [44]. The deconvolution of asymmetric XPS O 1s spectra is displayed in Fig. S7a, which can be assigned to defect oxygen (O_{defect}, B.E. of 531.6 eV) and lattice oxygen (O_{lattice}, B.E. of 528.7 eV) on the surface of M-ZnZrO_x samples [45]. It can be seen that the O_{defect}/(O_{lattice}+O_{defect}) ratio of Ga-ZnZrO_x (36.4 %) is higher than that of ZnZrO_x (27.1 %). In addition, XPS results show that the Ga (7.1 %) and Zn (18.4 %) concentration in the surface region is higher than the theoretical value (5 % and 13 %, respectively), suggesting that Ga-ZnZrO_x oxide is an imperfect solid solution in phase transition from skin layer to bulk [46].

Furthermore, the SiO₂/Al₂O₃ ratio of zeolite determines its acidity and thermal stability, which affects its catalytic activity [47,48]. Here, the SiO₂/Al₂O₃ ratio of ZSM-5 zeolites prepared with different silicon sources on the catalytic performance for CO₂ hydrogenation was optimized. Fig. 3c and Table S5 showed the results of bifunctional catalysts

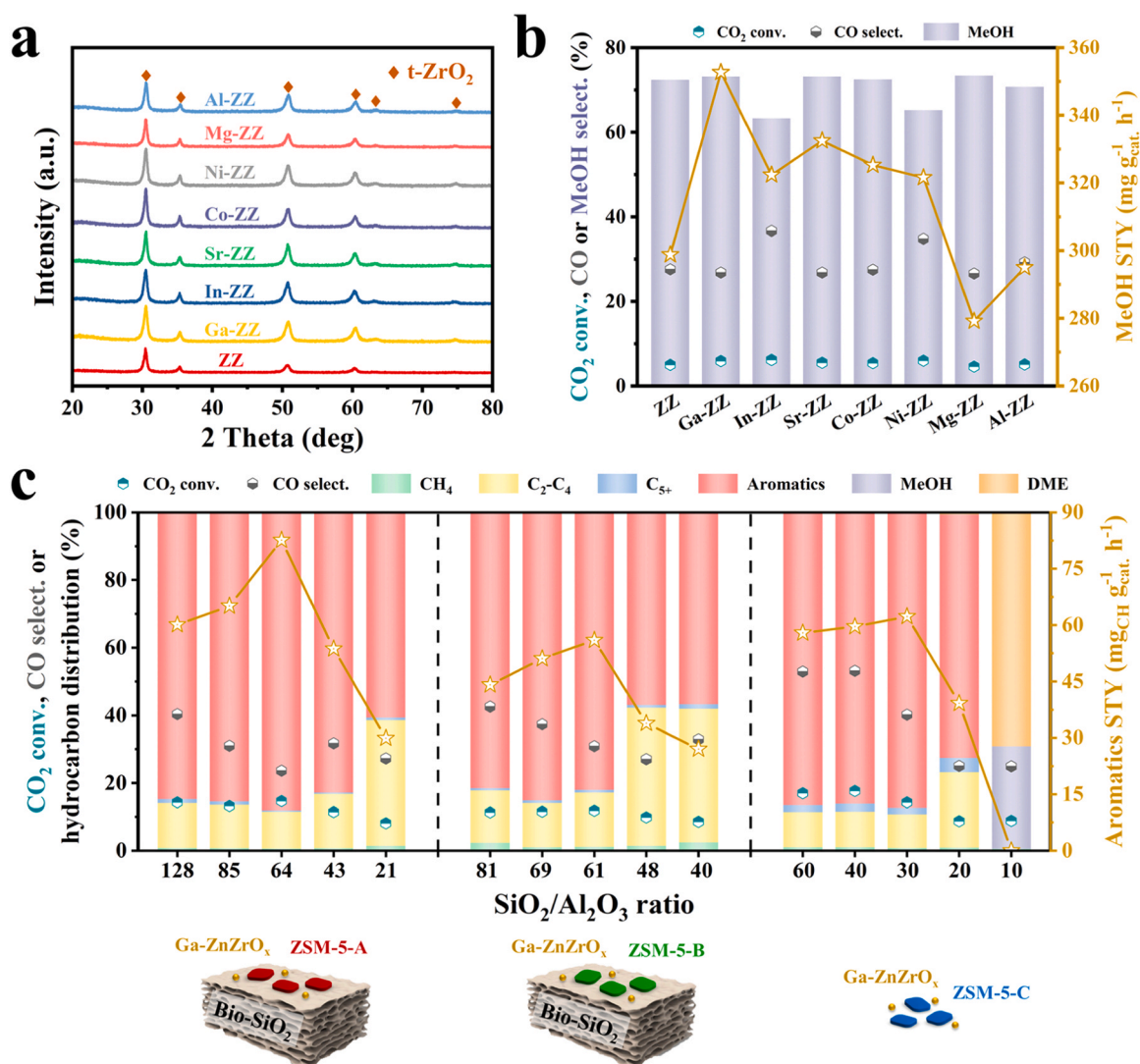


Fig. 3. (a) XRD patterns and (b) catalytic performances of various metal oxides for CO₂ hydrogenation to methanol. Reaction conditions: $T = 340\text{ }^{\circ}\text{C}$; $P = 3\text{ MPa}$; $\text{CO}_2/\text{H}_2 = 1:3$; $\text{GHSV} = 24,000\text{ mL g}_{\text{cat}}^{-1}\text{ h}^{-1}$. (c) Effect of different SiO₂/Al₂O₃ ratios of ZSM-5 over bifunctional catalysts (Ga-ZnZrO_x&ZSM-5) for CO₂ hydrogenation to aromatics. Reaction conditions: $T = 340\text{ }^{\circ}\text{C}$; $P = 3\text{ MPa}$; $\text{CO}_2/\text{H}_2 = 1:3$; $\text{GHSV} = 6000\text{ mL g}_{\text{cat}}^{-1}\text{ h}^{-1}$. Note: SiO₂/Al₂O₃ ratio consists of the silicon on both ZSM-5 and bio-SiO₂.

for CO₂ hydrogenation to aromatics at 340 °C, which contained Ga-ZnZrO_x catalyst and ZSM-5 zeolite with tunable SiO₂/Al₂O₃ ratio. Similarly, the aromatics STY of all three bifunctional catalysts composed of different zeolites first increased and then decreased with the decrease of SiO₂/Al₂O₃ ratio, while the trend of the by-product CO selectivity was the opposite. Specifically, the reduction of the SiO₂/Al₂O₃ ratio from 60 to 30 was accompanied by a decrease in CO selectivity of Ga-ZnZrO_x&ZSM-5-C catalysts from 52.9 % to 40.2 % and an increase in aromatics STY value to 62.3 mg_{CH} g_{cat}⁻¹ h⁻¹. However, as the SiO₂/Al₂O₃ ratio was further reduced to 10, methanol and dimethyl ether (DME) became the main products. This may be due to the low crystallinity and lack of active sites to catalyze methanol to hydrocarbons by C-C coupling over zeolite with too low SiO₂/Al₂O₃ ratio (Fig. S8) [49,50]. Strikingly, the Ga-ZnZrO_x&ZSM-5-A (SiO₂/Al₂O₃ ratio of 64) bifunctional catalysts integrated on the bio-SiO₂ platform achieved 88.1 % aromatics selectivity and 82.7 mg_{CH} g_{cat}⁻¹ h⁻¹ aromatics STY with CO selectivity suppressed to 23.6 % under the optimized conditions, which is superior to many reported catalysts for CO₂ hydrotreating to aromatics (Table 1).

The alkylbenzenes (e.g., trimethylbenzenes, tetramethylbenzenes, and pentamethylbenzene) have been proven to be the major carbon precursors for coke formation, which causes the deactivation of zeolite catalysts [55]. In addition, the spatial organization of the bifunctional catalysts can greatly affect the formation of coke on the catalysts [56]. The stability of the Ga-ZnZrO_x&ZSM-5 catalysts was investigated and the result is shown in Fig. 4. The CO selectivity was high during the reaction induction period and gradually decreased after a 30 h time-on-stream, indicating that the alkene and aromatic cycles on the zeolite become gradually dominant. In addition, it is also possible that the sintering of metal oxide nanoparticles reduced the CO selectivity due to the lower activity of larger metal particles for the water gas shift and reverse water gas shift (WGS/RWGS) reaction [57]. Under reaction conditions maintained for 150 h, there was no notable deactivation of the catalysts. Nevertheless, the high proximity of the two components of the Ga-ZnZrO_x&ZSM-5-C catalyst shortens the diffusion length, which greatly accelerates the transfer of macromolecular products and the formation of coke on the ZSM-5-C external surface. In contrast, the hierarchical structure of the bio-SiO₂ platform facilitates the diffusion of intermediate species and products, thereby enhancing the coking resistance of the Ga-ZnZrO_x&ZSM-5-A catalyst. Consequently, while the CO₂ conversion of Ga-ZnZrO_x&ZSM-5-C exhibited a decreasing trend, Ga-ZnZrO_x&ZSM-5-A maintained stability over 150 h on the stream. Besides, the coke species and its content over the used catalysts were examined by GC-MS and TG analyses, respectively (Fig. S9). It was observed that the coke content was only 3–5 % after 150 h of reaction (Fig. S9a). GC-MS spectra of the extracted coke solution showed that similar carbonaceous compounds (poly-branched aromatic hydrocarbons) were

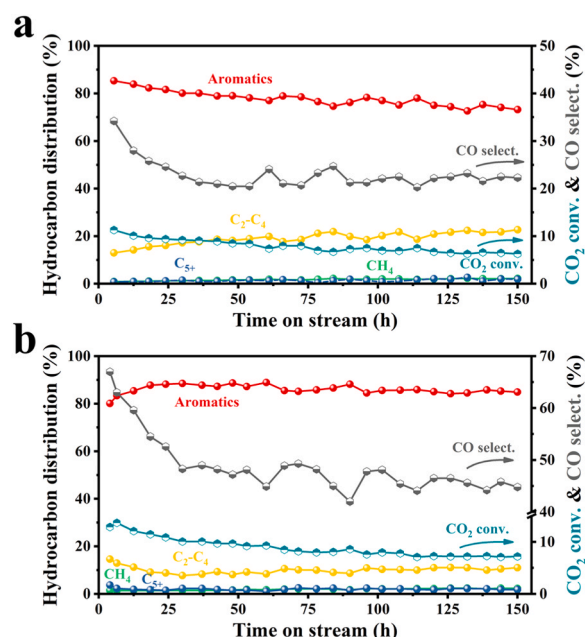


Fig. 4. Catalytic performance with time-on-stream of (a) Ga-ZnZrO_x&ZSM-5-A and (b) Ga-ZnZrO_x&ZSM-5-C. Reaction conditions: $T = 340$ °C; $P = 3$ MPa; CO₂: H₂ = 1:3; GHSV = 6000 mL g_{cat}⁻¹ h⁻¹.

retained in the used Ga-ZnZrO_x&ZSM-5-A and the used Ga-ZnZrO_x&ZSM-5-C catalysts (Fig. S9b). However, smaller organic molecules (i.e., xylene and trimethylbenzene) were not observed in the used Ga-ZnZrO_x&ZSM-5-A catalyst. This may be attributed to the hierarchical pore structure of the ZSM-5-A prepared from the biomass template, which promotes the diffusion of organic molecules. It is reasonable to conclude that (i) the *in-situ* silicon deposition released from rice husk on the surface of ZSM-5-A inhibited the deep alkylation of BTX and reduced the generation of coke precursors (vide infra); (ii) the hierarchical structure of bio-SiO₂ platform facilitated the diffusion of the generated intermediates and products, favoring the transfer of the internal coke precursors to the external surface of the zeolite, and preventing the accumulation of coke. Ultimately, the catalytic stability was enhanced.

3.3. Effect of *in-situ* silicon deposition on catalytic performance

Based on the above SiO₂/Al₂O₃ ratio studies, the bifunctional catalysts with the largest aromatics STY values (i.e., Ga-ZnZrO_x combined with ZSM-5-A with a SiO₂/Al₂O₃ ratio of 64, ZSM-5-B with a SiO₂/Al₂O₃

Table 1

Summary of the representative catalysts and their catalytic performance for aromatics synthesis from CO₂ hydrogenation based on the CO₂-MeOH mechanism.

Catalysts	T (°C)	P (MPa)	GHSV (mL g _{cat} ⁻¹ h ⁻¹)	X _{CO2} (%)	S _{CO} (%)	S _{Aro.} ^a (%)	STY _{Aro.} ^b (mg _{CH} g _{cat} ⁻¹ h ⁻¹)	BTX/Aro. (%)	Ref.
ZnZrO _x /ZSM-5	320	4	1200	14.1	44.0	73.0	9.6	11.0	[3]
ZnAlO _x &ZSM-5	320	3	2000	9.1	57.4	73.9	8.0	14.1	[4]
Cr ₂ O ₃ /H-ZSM-5	350	3	1200	33.6	41.2	70.5	23.3	n.a. ^c	[5]
ZnZrO _x /ZSM-5	320	3	2400	14.5	40.2	75.7	21.9	84.7	[17]
ZnZrO _x /ZSM-5	315	3	1020	17.5	23.8	60.3	11.4	20.4	[22]
ZnCrO _x -Zn/ZSM-5	320	5	3000	19.9	70.2	56.5	14.0	n.a.	[51]
ZnO/ZrO ₂ +ZSM-5	340	3	2700	9.1	42.5	70.0	13.8	12.0	[52]
ae-ZnZrO _x /HZSM-5	340	4	7200	15.9	34.0	76.0	80.0	31.4	[53]
ZnZrO _x -Zn/ZSM-5	320	3	4800	15.2	41.3	63.9	38.1	79.5	[54]
Ga-ZnZrO _x &Bio-ZSM-5	340	3	6000	14.7	23.6	88.1	82.7	45.2	This work

^a Aro. denotes aromatics and aromatics selectivity was calculated based on hydrocarbon product, excluding CO.

^b $STY_{Aro.} = \frac{M_{CH} * F_{CO_2} * X_{CO_2} * S_{Aro.} * (1 - S_{CO})}{V_m * g_{cat}}$, where M_{CH} is the molar mass of -CH-, F_{CO_2} is the gas volume flow rate of CO₂, V_m is the molar volume of the gas, g_{cat} is the mass of bifunctional catalysts.

^c n.a. means that the data is not available in the reference.

ratio of 61, and ZSM-5-C with a $\text{SiO}_2/\text{Al}_2\text{O}_3$ ratio of 30, respectively) were selected for the comparison of the catalytic performance and aromatics distribution, and the results are displayed in Fig. 5. Obviously, the CO_2 conversion of the Ga-ZnZrO_x&ZSM-5-A catalysts was increased from 11.8 % to 14.7 % compared to Ga-ZnZrO_x&ZSM-5-B, while the CO selectivity was reduced from 40.2 % to 23.6 % compared to Ga-ZnZrO_x&ZSM-5-C. Due to the identical metal oxide composition (i.e., Ga-ZnZrO_x), the significant decrease in CO selectivity is attributed to the ZSM-5-A favoring methanol consumption to hydrocarbon products (i.e., aromatics), which inhibits CO production from the competing RWGS reaction. Moreover, the multilayer structure of the bio- SiO_2 platform facilitated the surface diffusion of aromatic products, pulling methanol conversion [38]. On the other hand, the generated CO might also participate in C-C coupling reactions on zeolite. Thus, the aromatic STY of Ga-ZnZrO_x&ZSM-5-A was significantly increased to $82.7 \text{ mg}_{\text{CH}} \text{ g}_{\text{cat}}^{-1} \text{ h}^{-1}$, accompanied by an impressive 88.1 % aromatic selectivity. Fig. 5b-d showed the detailed aromatics distribution for CO_2 hydrogenation over bifunctional catalysts. It is noteworthy that the main aromatic products on the Ga-ZnZrO_x&ZSM-5-C catalysts were tri- and multiple-methyl benzene (~80 %), indicating the inevitable alkylation of BTX formed within the zeolite micropores to heavier aromatics during diffusion to the external surface acid sites of zeolite. In contrast, the products on the rice husk *in-situ* silicon-deposited ZSM-5-A and ZSM-5-B catalysts were dominated by xylene (~35 %) and trimethyl-benzene (~30 %). This difference can be attributed to the steric effects of ZSM-5, which restrict the formation of aromatic hydrocarbons larger than 1,2,4-trimethylbenzene. Therefore, we hypothesize that the *in-situ* deposition of silicon species, released from rice husks onto the ZSM-5 surface, is responsible for the modulation of the surface acidity (vide infra), leading to a high BTX selectivity. Furthermore, the surface diffusion of aromatic products among zeolite particles can be effectively weakened by using the hierarchically porous bio- SiO_2 platform to reduce the probability of BTX deep alkylation reactions.

It is well-known that acid properties, including acid type, acid strength, and acid density, are extremely important properties of zeolites as catalysts. Typically, the acidity of zeolites is produced by Brønsted acid sites (BAS) and Lewis acid sites (LAS), which are governed by the

structure, coordination state, and distribution of aluminum species in either framework or extra-framework positions [58]. Meanwhile, the acid strength of zeolites can be classified into strong, medium, and weak acids, which is closely related to the topology of zeolites, i.e., the bond angles of Si-O-Al bonds and the bond lengths of the Al-O bonds, etc. Here, the acid properties of the zeolites were determined by NH_3 -TPD and Py-FTIR. The acid site densities of the three zeolites were analyzed by deconvolution of NH_3 -TPD profiles in Fig. 6a. It should be noted that both ZSM-5-A and ZSM-5-B contain acid-free bio- SiO_2 platform, which leads to the relatively smaller acid density (Table 2). As shown in Fig. 6a, the desorption temperature decreases with the replacement of TEOS silicon species by rice husk silicon species. Specifically, the desorption corresponding to the weak-, medium- and strong-strength acid sites peaks at 180 °C, 242 °C and 370 °C for ZSM-5-B (containing silicon species only from rice husk), which were 12 °C, 23 °C and 20 °C lower than that of ZSM-5-C (containing silicon species only from TEOS), respectively. The desorption temperatures revealed that the acid strength decreased in the sequence of ZSM-5-C > ZSM-5-A > ZSM-5-B. Combined with the distribution of aromatic products in Fig. 5d, the higher acid strength of ZSM-C resulted in the BTX formed within the zeolite micropores being difficult to diffuse out of the catalyst bed from the zeolite surface, resulting in deep alkylation to heavier aromatics. Py-FTIR experiments were carried out to identify the acid site types of the ZSM-5 zeolites, as shown in Fig. 6b. The IR bands at around 1540 and

Table 2

Acid properties of ZSM-5 zeolites prepared with different silicon sources.

Zeolites	Acidity by strength (mmol g^{-1}) ^a				Acidity by type ^b
	Weak	Medium	Strong	Total	BAS/LAS
ZSM-5-A	0.11	0.08	0.12	0.32	2.52
ZSM-5-B	0.12	0.06	0.14	0.32	0.98
ZSM-5-C	0.17	0.16	0.07	0.40	9.55

Note:

^a By deconvolution of NH_3 -TPD profiles.

^b By deconvolution of Py-FTIR spectra.

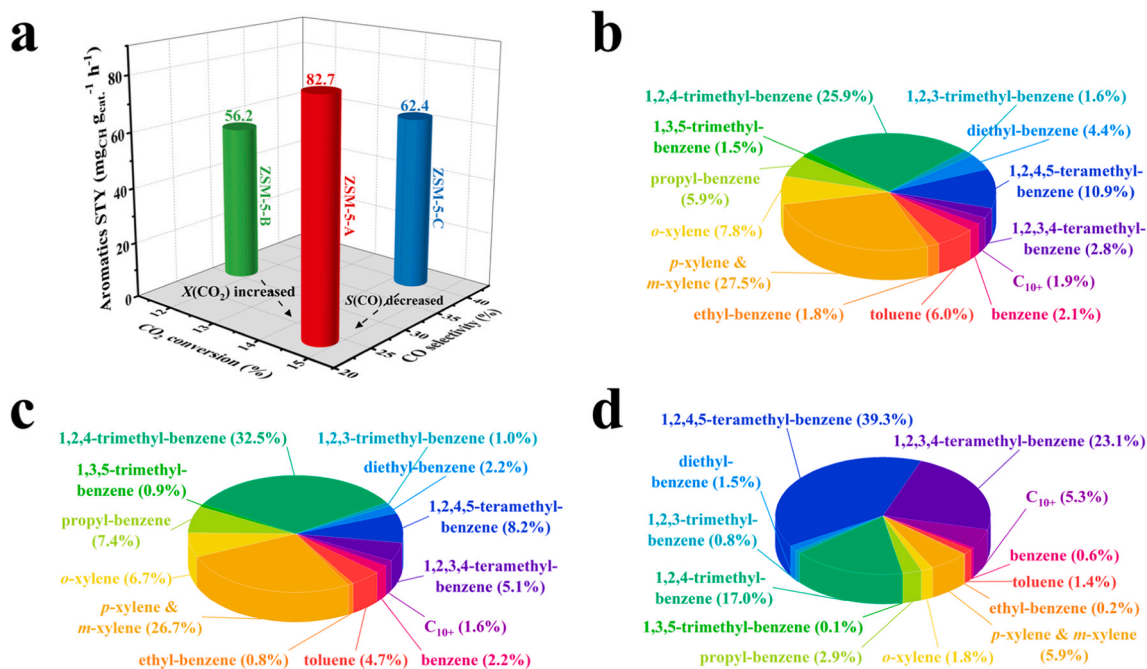


Fig. 5. (a) Hydroconversion of CO_2 over bifunctional catalysts with different ZSM-5 (optimal $\text{SiO}_2/\text{Al}_2\text{O}_3$ ratio for each zeolite). The detailed aromatic product distribution in CO_2 hydrogenation over (b) Ga-ZnZrO_x&ZSM-5-A, (c) Ga-ZnZrO_x&ZSM-5-B, and (d) Ga-ZnZrO_x&ZSM-5-C. Reaction conditions: $T = 340^\circ\text{C}$; $P = 3 \text{ MPa}$; $\text{CO}_2/\text{H}_2 = 1:3$; GHSV = $6000 \text{ mL g}_{\text{cat}}^{-1} \text{ h}^{-1}$.

1450 cm^{-1} were attributed to BAS and LAS, respectively [59]. Compared with the lower BAS/LAS value (0.98) of ZSM-5-B, ZSM-5-A has a desirable BAS/LAS value of 2.52, which promotes the cyclization of higher alkenes as well as hydrogen transfer of cycloalkanes to form aromatics. On the contrary, the higher BAS/LAS value (9.55) of ZSM-5-C exacerbated the deep reaction of light aromatic species. The above results illustrate that the involvement of silicon species released from rice husk in zeolite nucleation and crystallization alters the structure and coordination state of aluminum, thereby effectively modulating zeolitic acid properties. However, currently, we are unable to *in-situ* observe the release and deposition processes of silicon species from rice husks. Fig. 6

A key aspect of understanding the structure-activity relationship of ZSM-5 zeolites is the location of aluminum atoms in the catalyst framework [60]. Considering that the presence of aluminum is directly related to the acidity of zeolites and that the aluminum content is linearly related to the number of acid sites within a certain range. It was investigated to indirectly characterize the acid site distribution of the zeolites by detecting the distribution of aluminum by XPS. The XPS spectra shown in Fig. 7 illustrate that the peak intensity of the Si 2p signal on the exterior surface of these three zeolites is consistent, whereas the Al 2p signal of ZSM-5-A and ZSM-5-B exhibits weaker peak intensities and shift towards higher binding energies from 74.4 eV to 74.6 eV as compared to that of ZSM-5-C. This is indicative that the silicon species released from the rice husk would adsorb onto the external surface of ZSM-5 and convert to amorphous silicon during the calcination treatment, which covers part of the Al species on the external surface. It is widely accepted that the Al distribution in conventional ZSM-5 crystals is non-uniform, and Al is invariably concentrated in the rim portion of the crystals (*i.e.* aluminum zoning) [61], thus the acid sites are close to the external surface of the zeolite. Here, the distributions of Si and Al from the surface to the core of ZSM-5-A and ZSM-5-C samples were determined by XPS-sputtering, respectively (Fig. 8a and Fig. S10). As shown in Fig. 8a, a weak Al signal was detected on the ZSM-5-A surface (0 nm), and a stronger Al signal was detected at etching depths of 15 nm and above when Ar-ion was used to remove the ZSM-5-A surface layer. The $\text{SiO}_2/\text{Al}_2\text{O}_3$ ratios of ZSM-5-A and ZSM-5-C were calculated from the normalized peak area equations of the XPS-sputtering spectra. In Fig. 8b, ZSM-5-C shows an increase in $\text{SiO}_2/\text{Al}_2\text{O}_3$ ratio from the surface to the core as well as a minimum at 0 nm, indicating that Al is mainly distributed on the external surface of ZSM-5-C. On the contrary, ZSM-5-A shows an inverse Al-zoning distribution with a decrease in the $\text{SiO}_2/\text{Al}_2\text{O}_3$ ratio from the surface to the core as well as a minimum at 50 nm, suggesting that ZSM-5-A actually has an intrinsic inert external surface.

Additionally, variation in the external acid site of ZSM-5 was determined using a larger probe molecule, 2,6-di-tert-butyl-pyridine (2,6-DTBP), which cannot access the internal acid site of ZSM-5. As shown in Fig. 8c, the IR band at around 1615 cm^{-1} is attributed to the

adsorption of 2,6-DTBP at the external acid sites of the zeolite [62]. Obviously, the adsorption intensity of 2,6-DTBP on ZSM-5-A decreased to 29 % compared to ZSM-5-C (assumed to be 100 %), indicating a significantly decreased concentration of the externally accessible acid sites. Therefore, it can be deduced that the silicon species released from rice husk were *in-situ* deposited on the external surface of ZSM-5-A during the one-pot synthesis, resulting in the passivation of the external Brønsted acid sites of ZSM-5. This conclusion was fully consistent with the catalytic performance evaluation and the distribution of aromatic hydrocarbons in Fig. 5.

Moreover, the ^{27}Al MAS NMR was used to probe the distribution of aluminum (framework or non-framework sites) in different zeolites. As shown in Fig. 9a, the spectra can be deconvoluted into three distinct peaks near the chemical shift of 55, 46, and 0 ppm, which are associated with the tetrahedrally coordinated framework Al (Al_F), distorted-framework Al (Al_DF) and octahedrally coordinated extra-framework Al (Al_EF) species of ZSM-5 zeolites, respectively [63,64]. This fraction of extra-framework Al is most likely the result of post-synthesis methods such as ion exchange and high-temperature calcination, leading to hydrolysis of the framework Si-O-Al bonds and removal of aluminum from the framework [65]. It is worth noting that the distribution of Al atoms in the framework is also impacted by the silicon species released from rice husk, with the content of Al_EF decreasing from 12 % in ZSM-5-C to 7 % in ZSM-5-A. Typically, cyclization and hydrogen-transfer reactions of higher olefins resulting from C-C coupling are favored on the Al_F and Al_DF [66], while alkylation and deep alkylation of aromatics are preferred on the Al_EF (Fig. 9b). Therefore, the ^{27}Al MAS NMR results indicate that ZSM-5-A has a strong C-C coupling and aromatization ability due to the high Al_F content (72 %). In contrast, the low Al_EF content (7 %) can attenuate the deep alkylation of the resulting light aromatics, thus improving the BTX selectivity in total aromatics to 45 %. Although both ZSM-5-A and ZSM-5-B samples contain rice husk as a template, ZSM-5-B with the only silicon source from rice husk has weaker catalytic properties than ZSM-5-A due to the smaller BAS/LAS value (0.98 vs. 2.52) and the increased extra-framework Al (9 %).

Based on the above results, the introduction of rice husk has a significant impact on the nucleation and crystal growth process of zeolites. As shown in Fig. 9c, liquid silicon (TEOS) is rapidly hydrolyzed to nucleate with aluminum species to become the zeolite core prompted by a structure-directing agent (TPAOH). Then, the solid silicon (rice husk) in an alkaline solution slowly releases silicon species throughout the nucleation and crystallization process, which are *in-situ* deposited on the external surface of the zeolite core. In this case, the *in-situ* silicon species deposition forms an inverse aluminum zoning that passivates the acidic sites on the zeolitic external surface and also increases the number of tetrahedrally coordinated framework aluminum sites.

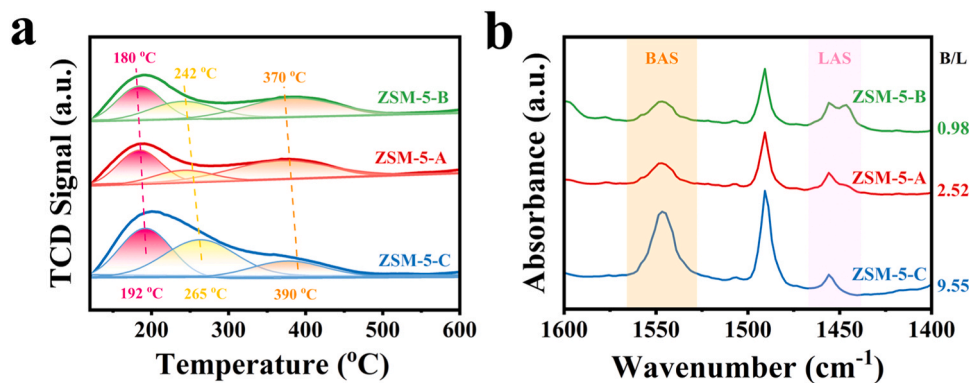


Fig. 6. (a) NH_3 -TPD profiles and (b) Py-FTIR spectra of ZSM-5 zeolites prepared with different silicon sources.

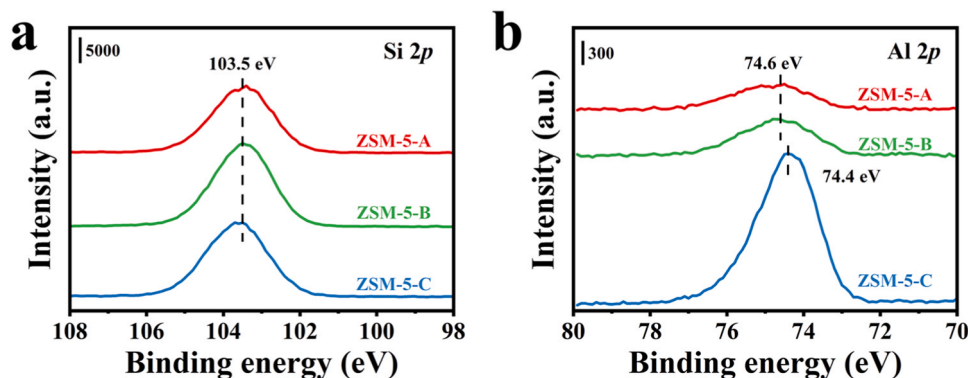


Fig. 7. (a) Si 2p and (b) Al 2p XPS spectra of ZSM-5 zeolites prepared with different silicon sources.

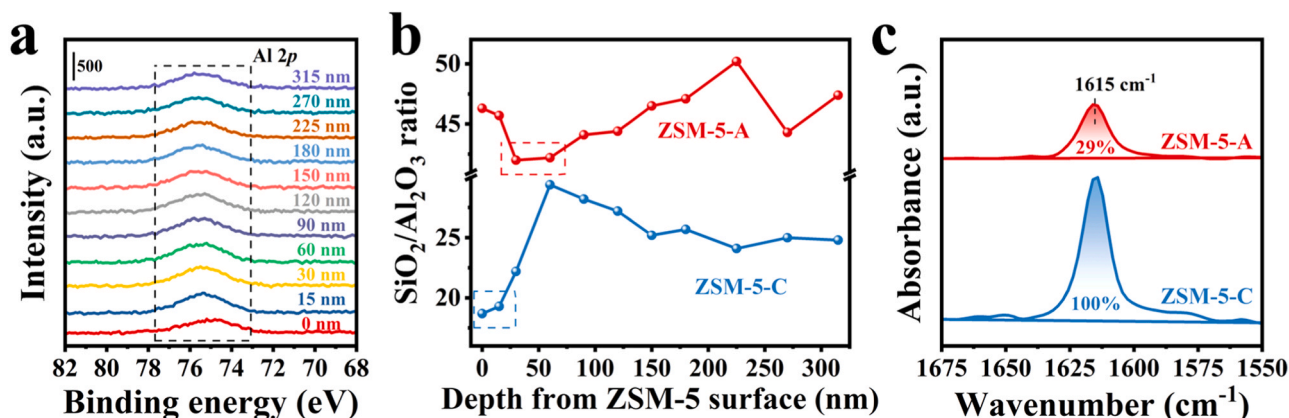


Fig. 8. (a) Al 2p XPS-sputtering spectra with a depth of 315 nm of ZSM-5-A and (b) dependence of the $\text{SiO}_2/\text{Al}_2\text{O}_3$ ratio on Ar-ion sputtering depth from ZSM-5 surface (based on the same sputtering conditions with an Ar-ion sputtering rate of 1.5 nm min^{-1} , the depths with the highest distribution of aluminum content are marked with dashed rectangles). (c) 2,6-DTBP-FTIR spectra of ZSM-5-A and ZSM-5-C to determine the acid sites on the exterior surface of zeolites.

3.4. Effect of proximity on the catalytic performance over bifunctional catalysts

For CO_2 hydrogenation to produce aromatics, the varied reactions should be carried out in order over the bifunctional catalysts, accompanied by rapid diffusion of intermediates from the metallic site to the zeolitic site. Therefore, the proximity between the two bifunctional sites (metal oxide and zeolite) also plays a crucial role in the tandem process. As aforementioned, the bio- SiO_2 could serve as a platform rather than a spacer (e.g., inert quartz sand) to adjust the distance between Ga-ZnZrO_x and ZSM-5. Thus, the distance between metal oxide and zeolite can be controlled by the amount of rice husk (or bio- SiO_2) and TEOS, which ultimately regulates the intimacy precisely (Fig. S11). For instance, when the addition of rice husk decreases and the addition of TEOS increases, the loadings of ZSM-5 and Ga-ZnZrO_x on the bio- SiO_2 platform increase, and the distance between the bifunctional components is closer; and vice versa. To understand the effect of proximity on CO_2 hydrogenation performance over bifunctional catalysts, the distance between Ga-ZnZrO_x and ZSM-5-A was evaluated. Although SEM and TEM are commonly used two-dimensional imaging instruments, the complexity of the three-dimensional structure of the actual bio- SiO_2 platform limits the use of these electron microscopes for direct measurement of distances between particles along the bio- SiO_2 surface. Therefore, the quantification of inter-particle distances can only be achieved by geometrical considerations to derive an equation to estimate the "average inter-particle distance", as a function of parameters such as the particle content, the particle size, homogeneity of the distribution of the particle, and surface area of the support [67]. Previously, resorting to the equation that was described by Yin *et al.* to

quantitatively estimate the distance (d) between particles, assuming perfectly uniform particle size and equidistant distribution of particles [68]. The average distance between metal oxides (d_m) and the average distance between zeolites (d_z) were calculated separately as follows:

$$d_m = \sqrt{\frac{\pi}{3\sqrt{3}} \times 10^{-3} \times \rho_m \times \left(\frac{100 - L_m}{L_m}\right) \times A_s \times r_m^3 - r_m} \quad (6)$$

$$d_z = \sqrt{\frac{\pi}{3\sqrt{3}} \times 10^{-3} \times \rho_z \times \left(\frac{100 - L_z}{L_z}\right) \times A_s \times r_z^3 - r_z} \quad (7)$$

where ρ_m is the density of metal oxides (5.85 g cm^{-3}), L_m is the loading amount of metal oxides (wt%, see Table S7), A_s is the specific surface area of the support (rice husk-derived bio- SiO_2 , $216.1 \text{ m}^2 \text{ g}^{-1}$) and r_m is the metal oxide's size in diameter (50 nm). ρ_z is the density of zeolites (0.68 g cm^{-3}), L_z is the loading amount of zeolites (wt%, see Table S7) and r_z is the zeolite's size in diameter (nm).

The distance between the metal oxide and zeolite was averaged as follows:

$$d_{\text{MO-ZEO}} = \sqrt{\frac{d_m^2 + d_z^2}{2}} \quad (8)$$

At the same time, the diffusion distance (L) of the reaction intermediate methanol generated on the oxide to find the acid site upstream was calculated for assessing the back-mixing degree based on the Péclet (Pe) number described by Li *et al.* [40]. Here, the back-mixing degree was evaluated using the reaction conditions of CO_2 hydrogenation to aromatics ($F_{\text{CO}_2/\text{H}_2} = 30 \text{ mL min}^{-1}$, $\text{CO}_2/\text{H}_2 = 1/3$, $P = 30 \text{ atm}$, and $T =$

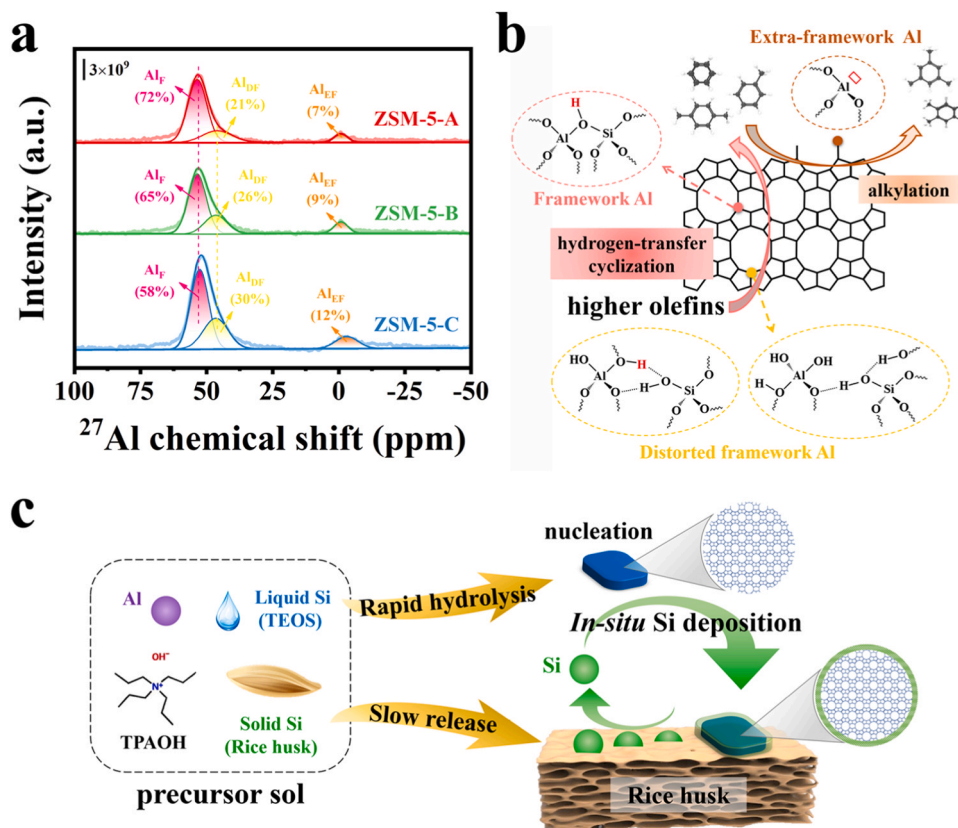


Fig. 9. (a) ^{27}Al MAS NMR spectra of ZSM-5 zeolites prepared with different silicon sources. (b) Schematic illustration of the cracking reaction of higher olefins on framework Al (both Al_F and Al_{DF}) and alkylation of light aromatics on extra-framework Al (Al_{EF}). (c) Schematic illustration of *in-situ* silicon species deposition on the zeolitic external surface.

613 K), and the diffusion range of methanol intermediate from Ga-ZnZrO_x to ZSM-5-A was calculated as $L = 0.43$ cm assuming $Pe = 1$. The proximity (P) of Ga-ZnZrO_x&ZSM-5-A catalyst was defined as the ratio of L to $d_{\text{MO-ZEO}}$, a dimensionless number:

$$\ln P = \ln \frac{L}{d_{\text{MO-ZEO}}} \quad (9)$$

The detailed calculations above can be found in the Supporting Information. The results of the calculations are shown in Table S8. It follows that the proximity P is a function of parameters such as particle loading amount, particle size, surface area of the support, and intermediate diffusion range. Therefore, the quantification of proximity applies to other reactions as well.

Herein, the $\text{SiO}_2/\text{Al}_2\text{O}_3$ ratio of ZSM-5-A zeolite was kept consistent while modulating the proximity (between the metal oxide and zeolite). The XRD, N_2 -physisorption, and XPS characterization results confirmed that Ga-ZnZrO_x&ZSM-5-A with varying proximity had consistent crystal structure, similar pore structure, and silicon-aluminum content on the zeolitic external surface (Figs. S12 and S13). Thus, other variables were excluded and only the effect of proximity on catalytic performance was investigated. As presented in Fig. 10, Ga-ZnZrO_x and ZSM-5-A have a large distance ($\ln P = 4.9$), leading to a relatively low CO_2 conversion (11.8 %) due to the far diffusion pathway for the methanol intermediate. Meanwhile, the hydrogen species formed during cyclization and dehydrogenation of higher olefins on zeolites to form aromatics could not be removed by transferring to separate Ga-ZnZrO_x to form gaseous hydrogen. This would lead to the accumulation of hydrogen species and subsequently form the undesired saturated alkanes (17.2 % selectivity without CO, see Fig. 10c (i)) [40]. The Ga-ZnZrO_x&ZSM-5-A ($\ln P = 5.1$) catalysts with moderate proximity showed increased CO_2 conversion (14.7 %) and significantly reduced CO selectivity (23.6 %), suggesting

that the consumption of methanol intermediates by zeolites favor the shift of the reaction equilibrium of CO_2 hydrogenation to methanol and suppressed the RWGS reaction. Therefore, an appropriate increase in proximity is beneficial for the aromatics selectivity and aromatics STY. Significantly, the Ga-ZnZrO_x&ZSM-5-A ($\ln P = 5.1$) catalyst achieved 88.1 % aromatics selectivity in a single-pass hydrogenation process, 45.2 % BTX selectivity for total aromatics, and $82.7 \text{ mg}_{\text{CH}} \text{ g}_{\text{cat}}^{-1} \text{ h}^{-1}$ for the STY of aromatics, which is the highest reported value for CO_2 hydrogenation (Table 1). Nevertheless, further reduction of the distance (*i.e.*, increasing the $\ln P$) between Ga-ZnZrO_x and ZSM-5-A resulted in a significant increase in CO selectivity to 65.4 % at almost identical CO_2 conversion as well as a decrease in aromatics STY to $39.8 \text{ mg}_{\text{CH}} \text{ g}_{\text{cat}}^{-1} \text{ h}^{-1}$. This indicates that high proximity accelerates the RWGS reaction and thus reduces the aromatics STY. Remarkably, the selectivity of BTX in total aromatics also decreases from 45.2 % to 8.3 % with increasing $\ln P$ (see Fig. 10b). It can be appreciated that excessive proximity results in a tendency for BTX to diffuse to adjacent zeolite surfaces, and thus undergo deep alkylation reactions at the acid sites to generate undesired heavy aromatics (see Fig. 10c (iii)). In addition, the metallic component can easily migrate to the protonic sites of zeolites and neutralize BAS, thus the integration between Ga-ZnZrO_x and ZSM-5 with a proper distance must be ensured [36]. At the same time, the conventional integration manners of bifunctional components were investigated, *i.e.*, dual-bed mode, granule stacking, and powder mixing manner (Fig. S14). Despite the increase in aromatics selectivity from dual-bed mode to powder mixing (*i.e.*, increased intimacy), the selectivity of BTX in total aromatics did not improve significantly (only 19.9 %), which was lower than that of the Ga-ZnZrO_x&ZSM-5-A catalysts integrated with bio- SiO_2 (45.2 %). In addition, varying the amount of quartz sand in a powder mixing manner was also ineffective in further improving BTX selectivity (Fig. S15). This means that conventional

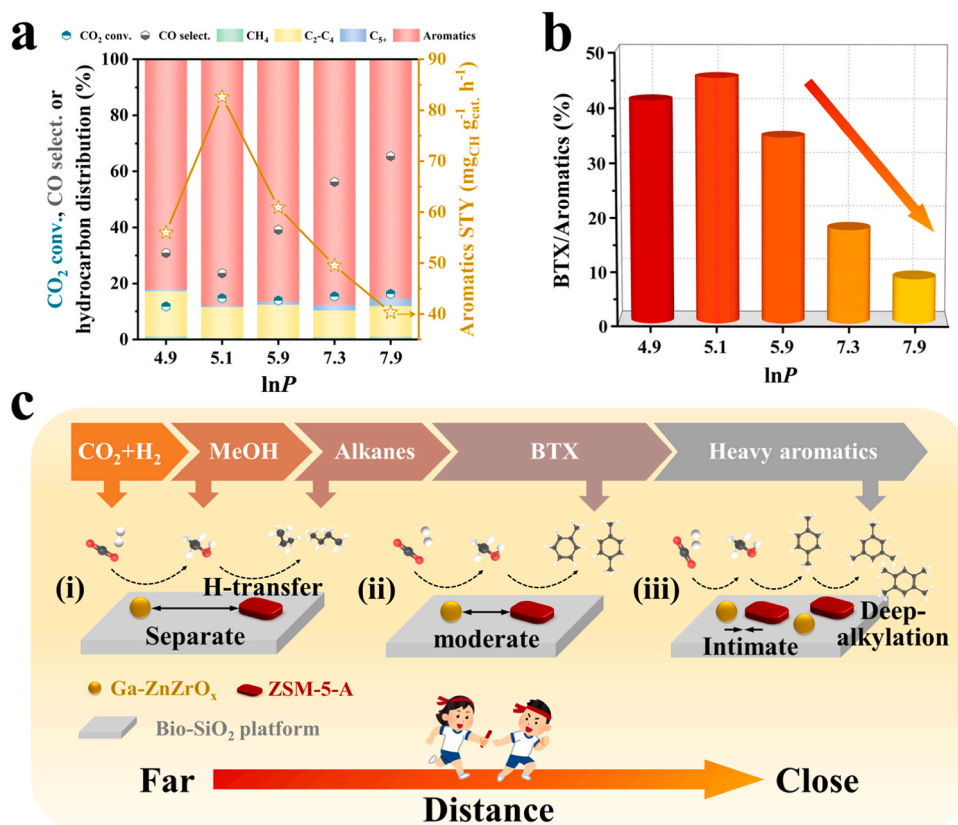


Fig. 10. Effect of different proximity over bifunctional catalysts in CO₂ hydrogenation: (a) CO₂ conversion, CO selectivity, and hydrocarbon distribution, (b) percentage of BTX in total aromatics, and (c) schematic illustration of the effect of Ga-ZnZrO_x&ZSM-5-A catalysts with varying proximity to aromatics using bio-SiO₂ as a platform (or separator). Reaction conditions: $T = 340\text{ }^{\circ}\text{C}$; $P = 3\text{ MPa}$; $\text{CO}_2\text{:H}_2 = 1\text{:}3$; GHSV = $6000\text{ mL g}_{\text{cat}}^{-1}\text{ h}^{-1}$.

quartz sand can not serve as a platform role to separate metal oxide and zeolite in the nanoscale range, being different from bio-SiO₂. Therefore, the introduction of rice husk in the catalyst fabrication could achieve dual benefits (modification of acidity and optimization of the spacing between Ga-ZnZrO_x and ZSM-5 on the bio-SiO₂ platform), which synergistically contributes to the enhanced BTX selectivity.

Furthermore, NH₃-TPD profiles (see Fig. 11) demonstrated that the peak positions of acid sites with different strengths all migrated to the low temperature and the acid density of ZSM-5-A decreased with decreasing lnP. Concretely, the desorption peaks corresponding to the weak-, medium- and strong-strength acid sites of ZSM-5-A (lnP = 5.1) were lower than those of ZSM-5-A (lnP = 7.9) by 13 °C, 45 °C, and 30 °C, respectively. In addition to being related to inter-particle distance, the

variation of zeolitic acid strength with proximity may also be related to the different sources and properties of the zeolitic silicon species, as the regulation of proximity was achieved by varying the addition of rice husk (natural solid silicon) and TEOS (liquid silicon) individually (see the Experimental section for details). The rice husk silicon species may have altered the structure and coordination state of aluminum in the zeolite framework. Besides, the loading amount of ZSM-5-A increases with the increase of lnP, leading to an increase in acid density for the same mass. Based on the abovementioned results, the BTX deep alkylation reaction is enhanced by simultaneously strengthened acidity and increased acid density. One should note that the rapid desorption after aromatics formation is critical for the formation of more BTX. Concurrently, the metal and acid sites must be well-located on the rice husk platform to ensure that the tandem reaction proceeds intentionally.

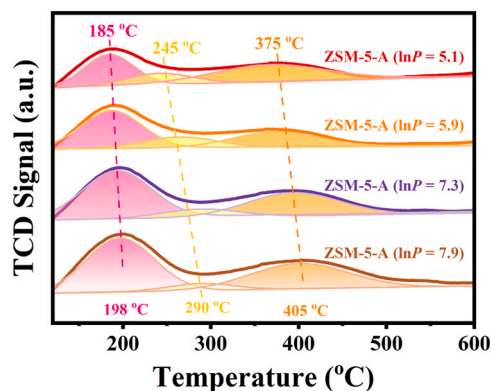


Fig. 11. NH₃-TPD profiles of ZSM-5-A zeolites prepared with different proximity.

3.5. Reaction mechanistic studies

In-situ DRIFTS analysis was used to monitor the surface species in CO₂ adsorption and activation on the catalyst to gain a better understanding of the variations and the unique behaviors of the Ga-ZnZrO_x&ZSM-5 catalyst in terms of CO₂ hydrogenation. Fig. 12a,c shows the CO₂ adsorption spectra before and after the desorption process (*viz.*, N₂ purge) on the Ga-ZnZrO_x&ZSM-5 catalyst. During the initial 1 min of CO₂ flow, the IR band intensities of carbonate (CO₃²⁻) species at 1600, 1490, 1385, and 1085 cm⁻¹ and bicarbonate (HCO₃⁻) species at 1210 and 1050 cm⁻¹ gradually increase and stabilize in the subsequent 30 min [69–71]. After switching from CO₂ to pure N₂ at 340 °C, the intensity of the carbonate and bicarbonate species decreased with the N₂ purge and then stabilized after 30 min. Surprisingly, the Ga-ZnZrO_x&ZSM-5 catalyst loaded on bio-SiO₂ platform still retained most of the chemisorbed carbonate intermediate species (Fig. 12a), whereas

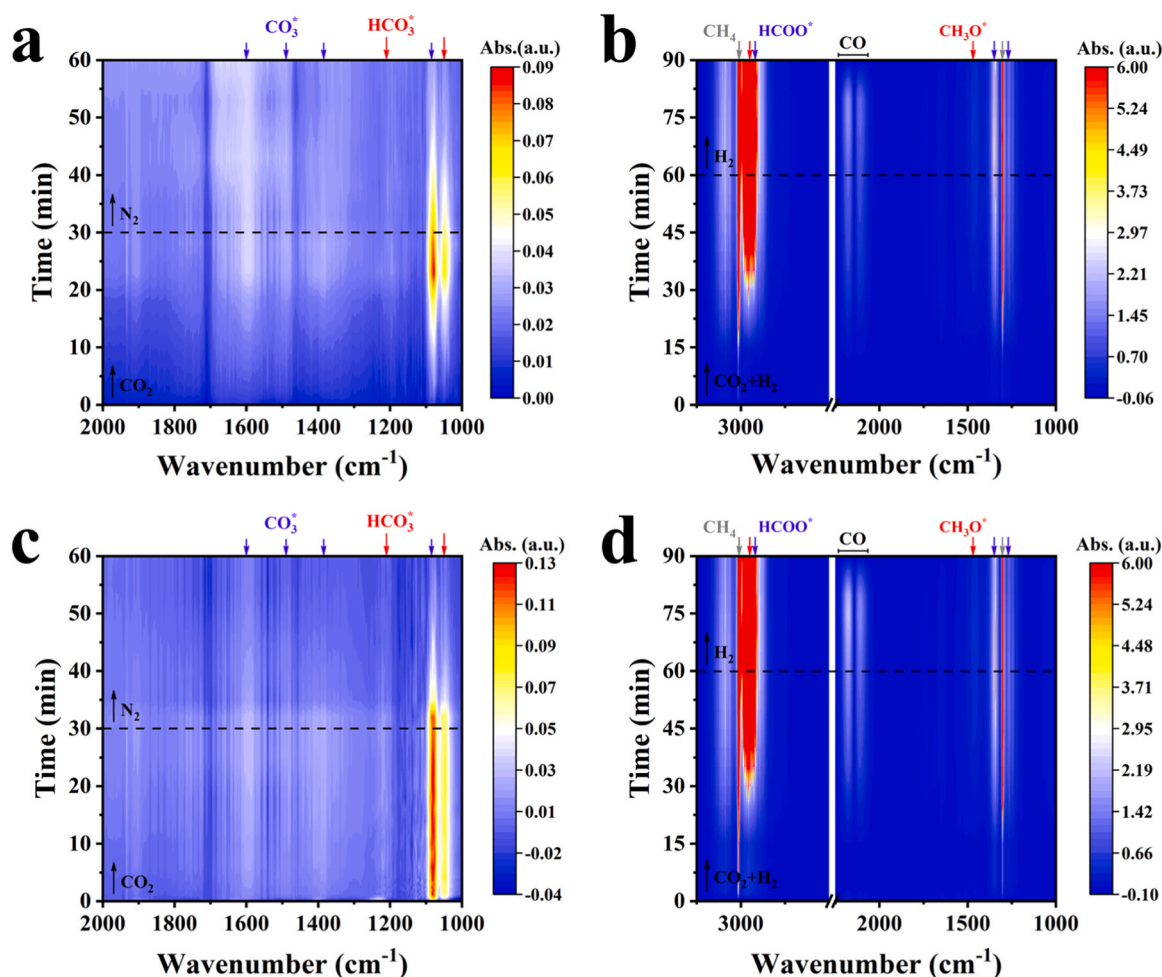


Fig. 12. *In-situ* DRIFT spectra of surface species formed in CO₂ adsorption and hydrogenation over (a,b) Ga-ZnZrO_x&ZSM-5-A and (c,d) Ga-ZnZrO_x&ZSM-5-C at 340 °C and 3 MPa.

only a small amount of chemisorbed carbonate species was retained on the Ga-ZnZrO_x&ZSM-5-C catalyst without the bio-SiO₂ platform (Fig. 12c). This may be due to the regulation of zeolitic acid properties by rice husk silicon species, and Ga-ZnZrO_x maintains a suitable distance from ZSM-5-A on the bio-SiO₂ platform, thus enhancing the chemisorption of carbonate species.

The CO₂ hydrogenation was performed on Ga-ZnZrO_x&ZSM-5 catalyst using a feed gas mixture (CO₂/H₂ = 1/3) at 340 °C and 3 MPa and DRIFTS were recorded as depicted in Fig. 12b,d. In the presence of H₂, the bicarbonate and carbonate species (*viz.*, HCO₃^{*} or CO₃^{*}) were not visible and two pivotal intermediates, namely formate (HCOO^{*}) and methoxy (CH₃O^{*}) appeared. From Fig. 12b,d, it can be observed that the IR bands centered at 2920, 1360, and 1270 cm⁻¹ belong to HCOO^{*} species and the IR bands centered at 2950 and 1470 cm⁻¹ belong to CH₃O^{*} species [46]. Therefore, the CO₂ hydrogenation over the Ga-ZnZrO_x&ZSM-5 catalysts follows the formate-methoxy reaction pathway. After 60 min of reaction, HCOO^{*} and CH₃O^{*} species gradually accumulated and signals belonging to CH₄ (at 3010 and 1300 cm⁻¹) and CO (at 2110–2170 cm⁻¹) were observed, while the peak intensities of CH₄ and CO further increased after switching from feed gas mixture to pure H₂, demonstrating that the intermediates (*viz.*, HCOO^{*} and CH₃O^{*}) were converted into the gaseous products over bifunctional catalyst. It is noteworthy that the peak intensity increase of CO for the Ga-ZnZrO_x&ZSM-5-A catalyst based on the bio-SiO₂ platform (Fig. 12b) is significantly smaller than that for the Ga-ZnZrO_x&ZSM-5-C catalyst without the bio-SiO₂ platform (Fig. 12d). This suggests that *in-situ* silicon-deposited ZSM-5-A zeolite from rice husk can drive the methanol

pathway to generate hydrocarbon products (*e.g.*, aromatics), while the competing RWGS reaction is effectively suppressed. This is consistent with the results obtained in the steady-state flow reactor (Fig. 5a).

4. Conclusion

In summary, we have synthesized and stabilized ZSM-5 particles on the rice husk-derived SiO₂ platform (rather than a spacer) together with metal oxide Ga-ZnZrO_x to form Ga-ZnZrO_x&ZSM-5 bifunctional catalysts. Particularly, it was demonstrated that the silicon species released from rice husk could be deposited on the zeolite external surface during the one-pot synthesis thereby reducing the extraframework and external surface aluminum as well as obtaining a weaker acid strength that is inactive for the secondary reaction of consuming BTX (*i.e.*, deep alkylation). After the regulation of acidity properties of ZSM-5 and proximity between the metal oxide and zeolite on bifunctional catalysts, CO₂ hydrogenation performance was assessed and optimized aiming to enhance the selectivity of BTX. Compared to zeolite without silicon source from rice husk, *in-situ* silicon deposited ZSM-5 assembled with Ga-ZnZrO_x on bio-SiO₂ with optimized proximity (*lnP* = 5.1) increased BTX selectivity (in total aromatics) from 10 % to 45.2 %, reduced CO selectivity (*i.e.*, RWGS reaction) from 40.2 % to 23.6 %, and achieved 88.1 % aromatics selectivity at 14.7 % CO₂ conversion at a single-pass process, which is superior to many conventional MO&ZEO catalysts. In addition, *in-situ* DRIFT results demonstrate that HCOO^{*} and CH₃O^{*} are key intermediates in CO₂ hydrogenation to aromatics over Ga-ZnZrO_x&ZSM-5 catalysts. It is believed that the regulation strategies on

acidity properties of ZSM-5 and proximity between the metal oxide and zeolite on a biologically derived platform could be highly desirable for enhancing BTX production from CO₂ thermal hydrogenation and paving the way for other tandem reactions.

CRedit authorship contribution statement

Yihua Yue: Writing – review & editing. **Jian Tian:** Writing – review & editing. **Jiechao Ma:** Methodology. **Shui Yang:** Methodology. **Wen Li:** Investigation. **Jiale Huang:** Project administration. **Qingbiao Li:** Writing – review & editing. **Guowu Zhan:** Conceptualization.

Declaration of Competing Interest

The authors declare that they have no known competing financial interests or personal relationships that could have appeared to influence the work reported in this paper.

Data availability

Data will be made available on request.

Acknowledgments

This work was financially supported by the National Natural Science Foundation of China (Nos. U21A20324, 22278167, and 22322806), the Natural Science Foundation of Fujian Province (No. 2021J06026), Fujian Provincial Chemistry Discipline Alliance, and we would like to thank the Instrumental Analysis Center of Huaqiao University for material characterization.

Appendix A. Supporting information

Supplementary data associated with this article can be found in the online version at [doi:10.1016/j.apcatb.2024.124158](https://doi.org/10.1016/j.apcatb.2024.124158).

References

- D. Wang, Z. Xie, M.D. Porosoff, J.G. Chen, Recent advances in carbon dioxide hydrogenation to produce olefins and aromatics, *Chem* 7 (2021) 2277–2311.
- R.P. Ye, J. Ding, W. Gong, M.D. Argyle, Q. Zhong, Y. Wang, C.K. Russell, Z. Xu, A. G. Russell, Q. Li, M. Fan, Y.G. Yao, CO₂ hydrogenation to high-value products via heterogeneous catalysis, *Nat. Commun.* 10 (2019) 5698.
- Z. Li, Y. Qu, J. Wang, H. Liu, M. Li, S. Miao, C. Li, Highly selective conversion of carbon dioxide to aromatics over tandem catalysts, *Joule* 3 (2019) 570–583.
- Y. Ni, Z. Chen, Y. Fu, Y. Liu, W. Zhu, Z. Liu, Selective conversion of CO₂ and H₂ into aromatics, *Nat. Commun.* 9 (2018) 3457.
- Y. Wang, L. Tan, M. Tan, P. Zhang, Y. Fang, Y. Yoneyama, G. Yang, N. Tsubaki, Rationally designing bifunctional catalysts as an efficient strategy to boost CO₂ hydrogenation producing value-added aromatics, *ACS Catal.* 9 (2019) 895–901.
- Y. Wang, S. Kazumi, W. Gao, X. Gao, H. Li, X. Guo, Y. Yoneyama, G. Yang, N. Tsubaki, Direct conversion of CO₂ to aromatics with high yield via a modified Fischer-Tropsch synthesis pathway, *Appl. Catal. B: Environ.* 269 (2020) 118792.
- X. Cui, P. Gao, S. Li, C. Yang, Z. Liu, H. Wang, L. Zhong, Y. Sun, Selective production of aromatics directly from carbon dioxide hydrogenation, *ACS Catal.* 9 (2019) 3866–3876.
- P. Gao, S. Li, X. Bu, S. Dang, Z. Liu, H. Wang, L. Zhong, M. Qiu, C. Yang, J. Cai, W. Wei, Y. Sun, Direct conversion of CO₂ into liquid fuels with high selectivity over a bifunctional catalyst, *Nat. Chem.* 9 (2017) 1019–1024.
- J. Wei, Q. Ge, R. Yao, Z. Wen, C. Fang, L. Guo, H. Xu, J. Sun, Directly converting CO₂ into a gasoline fuel, *Nat. Commun.* 8 (2017) 15174.
- A. Noreen, M. Li, Y. Fu, C.C. Amoo, J. Wang, E. Maturura, C. Du, R. Yang, C. Xing, J. Sun, One-pass hydrogenation of CO₂ to multibranched isoparaffins over bifunctional zeolite-based catalysts, *ACS Catal.* 10 (2020) 14186–14194.
- D. Cai, Y. Cai, K.B. Tan, G. Zhan, Recent advances of indium oxide-based catalysts for CO₂ hydrogenation to methanol: experimental and theoretical, *Materials* 16 (2023) 2803.
- J. Zhong, X. Yang, Z. Wu, B. Liang, Y. Huang, T. Zhang, State of the art and perspectives in heterogeneous catalysis of CO₂ hydrogenation to methanol, *Chem. Soc. Rev.* 49 (2020) 1385–1413.
- X. Shang, G. Liu, X. Su, Y. Huang, T. Zhang, Preferential synthesis of toluene and xylene from CO₂ hydrogenation in the presence of benzene through an enhanced coupling reaction, *ACS Catal.* 12 (2022) 13741–13754.
- S. De, A. Dokania, A. Ramirez, J. Gascon, Advances in the design of heterogeneous catalysts and thermocatalytic processes for CO₂ Utilization, *ACS Catal.* 10 (2020) 14147–14185.
- D. Goud, R. Gupta, R. Maligal-Ganesh, S.C. Peter, Review of catalyst design and mechanistic studies for the production of olefins from anthropogenic CO₂, *ACS Catal.* 10 (2020) 14258–14282.
- K.R.G. Lim, S.K. Kaiser, H. Wu, S. Garg, M. Perxès Perich, J.E.S. van der Hoeven, M. Aizenberg, J. Aizenberg, Nanoparticle proximity controls selectivity in benzaldehyde hydrogenation, *Nat. Catal.* (2024).
- H. Tian, H. He, J. Jiao, F. Zha, X. Guo, X. Tang, Y. Chang, Tandem catalysts composed of different morphology HZSM-5 and metal oxides for CO₂ hydrogenation to aromatics, *Fuel* 314 (2022) 123119.
- J. R. Yao, Q. Ge, D. Xu, C. Fang, J. Zhang, H. Xu, J. Sun, Precisely regulating Brønsted acid sites to promote the synthesis of light aromatics via CO₂ hydrogenation, *Appl. Catal. B: Environ.* 283 (2021) 119648.
- Y. Wang, W. Gao, S. Kazumi, H. Li, G. Yang, N. Tsubaki, Direct and oriented conversion of CO₂ into value-added aromatics, *Chemistry* 25 (2019) 5149–5153.
- Y. Jiao, L. Forster, S. Xu, H. Chen, J. Han, X. Liu, Y. Zhou, J. Liu, J. Zhang, J. Yu, C. D'Agostino, X. Fan, Creation of Al-enriched mesoporous ZSM-5 nanoboxes with high catalytic activity: converting tetrahedral extra-framework Al into framework sites by post treatment, *Angew. Chem. Int. Ed.* 59 (2020) 19478–19486.
- C. Wang, L. Zhang, X. Huang, Y. Zhu, G.K. Li, Q. Gu, J. Chen, L. Ma, X. Li, Q. He, J. Xu, Q. Sun, C. Song, M. Peng, J. Sun, D. Ma, Maximizing sinusoidal channels of HZSM-5 for high shape-selectivity to p-xylene, *Nat. Commun.* 10 (2019) 4348.
- T. Wang, C. Yang, P. Gao, S. Zhou, S. Li, H. Wang, Y. Sun, ZnZrO_x integrated with chain-like nanocrystal HZSM-5 as efficient catalysts for aromatics synthesis from CO₂ hydrogenation, *Appl. Catal. B: Environ.* 286 (2021) 119929.
- R. Lv, Hejin Tangbo, Qiuying Wang, S. Xiang, Properties and characterization of modified HZSM-5 zeolites, *J. Nat. Gas. Chem.* 12 (2003) 56–62.
- C. Mille, E.C. Tyrode, R.W. Corkery, Inorganic chiral 3-D photonic crystals with bicontinuous gyroid structure replicated from butterfly wing scales, *Chem. Commun.* 47 (2011) 9873–9875.
- W. Li, K. Wang, G. Zhan, J. Huang, Q. Li, Hydrogenation of CO₂ to dimethyl ether over tandem catalysts based on biotemplated hierarchical ZSM-5 and Pd/ZnO, *ACS Sustain. Chem. Eng.* 8 (2020) 14058–14070.
- J. Ma, H. Fan, H. Tian, X. Ren, C. Wang, S. Gao, W. Wang, Ultrahigh sensitivity and selectivity chlorine gas sensing of In₂O₃ hollow microtubules by bio-template method with degreasing cotton, *Sens. Actuators B: Chem.* 262 (2018) 17–25.
- X. Jiang, Y. Liu, H. Hao, Y. Xu, J. Huang, D. Sun, Q. Li, Rape pollen-templated synthesis of C,N self-doped hierarchical TiO₂ for selective hydrogenation of 1,3-butadiene, *ACS Sustain. Chem. Eng.* 6 (2018) 882–888.
- Z.Y. Ju, L.N. Song, M.B. Chong, D.G. Cheng, Y. Hou, X.M. Zhang, Q.H. Zhang, L. H. Ren, Selective aerobic oxidation of C_{3sp}-H bonds catalyzed by yeast-derived nitrogen, phosphorus, and oxygen codoped carbon materials, *J. Org. Chem.* 87 (2022) 3978–3988.
- J. Huang, L. Lin, D. Sun, H. Chen, D. Yang, Q. Li, Bio-inspired synthesis of metal nanomaterials and applications, *Chem. Soc. Rev.* 44 (2015) 6330–6374.
- P. Tian, G. Zhan, J. Tian, K.B. Tan, M. Guo, Y. Han, T. Fu, J. Huang, Q. Li, Direct CO₂ hydrogenation to light olefins over ZnZrO_x mixed with hierarchically hollow SAPO-34 with rice husk as green silicon source and template, *Appl. Catal. B: Environ.* 315 (2022) 121572.
- W. Li, G. Zhan, X. Liu, Y. Yue, K.B. Tan, J. Wang, J. Huang, Q. Li, Assembly of ZnZrO_x and ZSM-5 on hierarchically porous bio-derived SiO₂ platform as bifunctional catalysts for CO₂ hydrogenation to aromatics, *Appl. Catal. B: Environ.* 330 (2023) 122575.
- W.-T. Tsai, Y.-Q. Lin, H.-J. Huang, Valorization of rice husk for the production of porous biochar materials, *Fermentation* 7 (2021) 70.
- K. Cheng, Y. Li, J. Kang, Q. Zhang, Y. Wang, Selectivity control by relay catalysis in CO and CO₂ hydrogenation to multicarbon compounds, *Acc. Chem. Res.* (2024).
- W. Zhou, K. Cheng, J. Kang, C. Zhou, V. Subramanian, Q. Zhang, Y. Wang, New horizon in C1 chemistry: breaking the selectivity limitation in transformation of syngas and hydrogenation of CO₂ into hydrocarbon chemicals and fuels, *Chem. Soc. Rev.* 48 (2019) 3193–3228.
- Y. Wang, G. Wang, L.I. van der Wal, K. Cheng, Q. Zhang, K.P. de Jong, Y. Wang, Visualizing element migration over bifunctional metal-zeolite catalysts and its impact on catalysis, *Angew. Chem. Int. Ed. Engl.* 60 (2021) 17735–17743.
- Y. Li, L. Zeng, G. Pang, X. Wei, M. Wang, K. Cheng, J. Kang, J.M. Serra, Q. Zhang, Y. Wang, Direct conversion of carbon dioxide into liquid fuels and chemicals by coupling green hydrogen at high temperature, *Appl. Catal. B: Environ.* 324 (2023) 122299.
- X. Qi, V. Vattipalli, P.J. Dauenhauer, W. Fan, Silica nanoparticle mass transfer fins for MFI composite materials, *Chem. Mater.* 30 (2018) 2353–2361.
- B. Chen, S. Yang, L. Shang, Y. Wu, Y. Wang, J. Tian, J. Huang, X. Zhang, Q. Li, G. Zhan, Catalytic pyrolysis of biomass to aromatics over bifunctional Ni/ZSM-5 catalysts assembled on rice husk-derived silica platform, *Chem. Catal.* (2024).
- J. Sun, C. Mu, D. Guo, Y. Zhao, S. Wang, X. Ma, Effects of intimacy between acid and metal sites on the isomerization of n-C16 at the large/minor nanoscale and atomic scale, *ACS Catal.* 12 (2022) 4092–4102.
- Y. Li, M. Wang, S. Liu, F. Wu, Q. Zhang, S. Zhang, K. Cheng, Y. Wang, Distance for communication between metal and acid sites for syngas conversion, *ACS Catal.* 12 (2022) 8793–8801.
- Y. Xu, G. Ma, J. Bai, Y. Du, C. Qin, M. Ding, Yolk@shell FeMn@hollow HZSM-5 nanoreactor for directly converting syngas to aromatics, *ACS Catal.* 11 (2021) 4476–4485.

- [42] T. Fu, Y. Guo, Z. Li, G. Zhan, Selective conversion of methanol to aromatics with superior catalytic stability by relay catalysis over quadruple ZSM-5 sequence beds with gradient-increasing acidity, *Fuel* 315 (2022) 123241.
- [43] F. Sha, C. Tang, S. Tang, Q. Wang, Z. Han, J. Wang, C. Li, The promoting role of Ga in ZnZrO_x solid solution catalyst for CO_2 hydrogenation to methanol, *J. Catal.* 404 (2021) 383–392.
- [44] J. Wang, C. Tang, G. Li, Z. Han, Z. Li, H. Liu, F. Cheng, C. Li, High-performance MaZrO_x ($\text{Ma} = \text{Cd}, \text{Ga}$) solid-solution catalysts for CO_2 hydrogenation to methanol, *ACS Catal.* 9 (2019) 10253–10259.
- [45] Z. Cai, J. Dai, W. Li, K.B. Tan, Z. Huang, G. Zhan, J. Huang, Q. Li, Pd Supported on MIL-68(In)-derived In_2O_3 nanotubes as superior catalysts to boost CO_2 hydrogenation to methanol, *ACS Catal.* 10 (2020) 13275–13289.
- [46] J. Wang, G. Li, Z. Li, C. Tang, Z. Feng, H. An, H. Liu, T. Liu, C. Li, A highly selective and stable ZnO-ZrO_2 solid solution catalyst for CO_2 hydrogenation to methanol, *Sci. Adv.* 3 (2017) e1701290.
- [47] W. Gao, L. Guo, Q. Wu, C. Wang, X. Guo, Y. He, P. Zhang, G. Yang, G. Liu, J. Wu, N. Tsubaki, Capsule-like zeolite catalyst fabricated by solvent-free strategy for para-Xylene formation from CO_2 hydrogenation, *Appl. Catal. B: Environ.* 303 (2022) 120906.
- [48] Y. Xue, J. Li, P. Wang, X. Cui, H. Zheng, Y. Niu, M. Dong, Z. Qin, J. Wang, W. Fan, Regulating Al distribution of ZSM-5 by Sn incorporation for improving catalytic properties in methanol to olefins, *Appl. Catal. B: Environ.* 280 (2021) 119391.
- [49] A.A. Rowanaghi, F. Rezaei, M. Stante, J. Hedlund, Selective dehydration of methanol to dimethyl ether on ZSM-5 nanocrystals, *Appl. Catal. B: Environ.* (2012) 119–120, 56–61.
- [50] S. Al-Nahari, E. Dib, C. Cammarano, E. Saint-Germes, D. Massiot, V. Sarou-Kanian, B. Alonso, Impact of mineralizing agents on aluminum distribution and acidity of ZSM-5 zeolites, *Angew. Chem. Int. Ed.* 62 (2023).
- [51] J. Zhang, M. Zhang, S. Chen, X. Wang, Z. Zhou, Y. Wu, T. Zhang, G. Yang, Y. Han, Y. Tan, Hydrogenation of CO_2 into aromatics over a ZnCrO_x -zeolite composite catalyst, *Chem. Commun.* 55 (2019) 973–976.
- [52] X. Zhang, A. Zhang, X. Jiang, J. Zhu, J. Liu, J. Li, G. Zhang, C. Song, X. Guo, Utilization of CO_2 for aromatics production over ZnO/ZrO_2 -ZSM-5 tandem catalyst, *J. CO₂ Util.* 29 (2019) 140–145.
- [53] C. Zhou, J. Shi, W. Zhou, K. Cheng, Q. Zhang, J. Kang, Y. Wang, Highly active ZnO-ZrO_2 aerogels integrated with H-ZSM-5 for aromatics synthesis from carbon dioxide, *ACS Catal.* 10 (2019) 302–310.
- [54] H. Tian, J. Jiao, F. Zha, X. Guo, X. Tang, Y. Chang, H. Chen, Hydrogenation of CO_2 into aromatics over ZnZrO-Zn/HZSM-5 composite catalysts derived from ZIF-8, *Catal. Sci. Technol.* 12 (2022) 799–811.
- [55] L. Zhang, T. Fu, J. Shao, Y. Guo, H. Li, Y. Han, G. Zhan, Z. Li, Strengthening catalytic synergy of two function-complementary ZSM-5 by optimizing their spatial organizations in fixed-bed reactor to boost methanol aromatization, *Microporous Mesoporous Mater.* 337 (2022) 111953.
- [56] H. An, F. Zhang, Z. Guan, X. Liu, F. Fan, C. Li, Investigating the coke formation mechanism of H-ZSM-5 during methanol dehydration using operando UV-Raman spectroscopy, *ACS Catal.* 8 (2018) 9207–9215.
- [57] N. Li, F. Jiao, X. Pan, Y. Ding, J. Feng, X. Bao, Size effects of ZnO nanoparticles in bifunctional catalysts for selective syngas conversion, *ACS Catal.* 9 (2018) 960–966.
- [58] M. Hu, C. Wang, Y. Chu, Q. Wang, S. Li, J. Xu, F. Deng, Unravelling the reactivity of framework lewis acid sites towards methanol activation on H-ZSM-5 zeolite with solid-state NMR spectroscopy, *Angew. Chem. Int. Ed.* 61 (2022) e202207400.
- [59] W. Li, K. Wang, G. Zhan, J. Huang, Q. Li, Design and synthesis of bioinspired ZnZrO_x -Bio-ZSM-5 integrated nanocatalysts to boost CO_2 hydrogenation to light olefins, *ACS Sustain. Chem. Eng.* 9 (2021) 6446–6458.
- [60] K. Chen, Z. Gan, S. Horstmeier, J.L. White, Distribution of aluminum species in zeolite catalysts: ^{27}Al NMR of framework, partially-coordinated framework, and non-framework moieties, *J. Am. Chem. Soc.* 143 (2021) 6669–6680.
- [61] R. von Ballmoos, W.M. Meier, Zoned aluminium distribution in synthetic zeolite ZSM-5, *Nature* 289 (1981) 782–783.
- [62] H. Wang, P. Gao, S. Li, T. Wang, C. Yang, J. Li, T. Lin, L. Zhong, Y. Sun, Bifunctional catalysts with versatile zeolites enable unprecedented para-xylene productivity for syngas conversion under mild conditions, *Chem. Catal.* (2022).
- [63] M. Ravi, V.L. Sushkevich, J.A. van Bokhoven, Towards a better understanding of Lewis acidic aluminium in zeolites, *Nat. Mater.* 19 (2020) 1047–1056.
- [64] R. Liu, B. Fan, W. Zhang, L. Wang, L. Qi, Y. Wang, S. Xu, Z. Yu, Y. Wei, Z. Liu, Increasing the number of aluminum atoms in T₃ sites of a mordenite zeolite by low-pressure SiCl_4 treatment to catalyze dimethyl ether carbonylation, *Angew. Chem. Int. Ed.* 61 (2022) e202116990.
- [65] K. Chen, X. Wu, J. Zhao, H. Zhao, A. Li, Q. Zhang, T. Xia, P. Liu, B. Meng, W. Song, X. Zhu, H. Liu, X. Gao, C. Xu, B. Shen, Organic-free modulation of the framework Al distribution in ZSM-5 zeolite by magnesium participated synthesis and its impact on the catalytic cracking reaction of alkanes, *J. Catal.* 413 (2022) 735–750.
- [66] Z. Xu, T. Fu, Y. Han, Z. Li, G. Zhan, Facilely adjusting acidity features of zeolites by steaming treatment for enhanced methanol conversion to aromatics: A mechanism study, *Fuel* 349 (2023) 128671.
- [67] J.C. Meier, C. Galeano, I. Katsounaros, J. Witte, H.J. Bongard, A.A. Topalov, C. Baldizzone, S. Mezzavilla, F. Schuth, K.J.J. Mayrhofer, Design criteria for stable Pt/C fuel cell catalysts, *Beilstein J. Nanotechnol.* 5 (2014) 44–67.
- [68] P. Yin, S. Hu, K. Qian, Z. Wei, L.L. Zhang, Y. Lin, W. Huang, H. Xiong, W.X. Li, H. W. Liang, Quantification of critical particle distance for mitigating catalyst sintering, *Nat. Commun.* 12 (2021) 4865.
- [69] T. Huang, R. Wang, J. Zhang, J. Wang, H. Ge, J. Ren, Z. Zheng, Cyano group modified graphitic carbon nitride supported Ru nanoparticles for enhanced CO_2 methanation, *Chem. Eng. J.* 467 (2023) 143469.
- [70] Y. Yue, Z. Huang, D. Cai, S. Ullah, A.-R. Ibrahim, X. Yang, J. Huang, G. Zhan, Fabrication of multi-layered $\text{Co}_3\text{O}_4/\text{ZnO}$ nanocatalysts for spectroscopic visualization: effect of spatial positions on CO_2 hydrogenation performance, *Fuel* 321 (2022) 124042.
- [71] J. Zuo, W. Chen, J. Liu, X. Duan, L. Ye, Y. Yuan, Selective methylation of toluene using CO_2 and H_2 to para-xylene, *Sci. Adv.* 6 (2020) eaba5433.